REPORT DOCUMENTATION PAGE	Form Approved OMB NO. 0704-0188

1. REPORT DATE (DD-MM-YYYY)	2. REPORT TYPE	3. DATES COVERED (From - To)
19-11-2015	Final Report	1-Oct-2012 - 30-Jun-2015

4. TITLE AND SUBTITLE
Final Report: Theoretical Studies of Oxygen Reduction and Proton Transfer in SOFCs and Nerve Agents on Selected Surfaces

5a. CONTRACT NUMBER
W911NF-12-1-0501

5b. GRANT NUMBER

5c. PROGRAM ELEMENT NUMBER
611102

6. AUTHORS
Changyong Qin, Jerry Whitten

5d. PROJECT NUMBER

5e. TASK NUMBER

5f. WORK UNIT NUMBER

7. PERFORMING ORGANIZATION NAMES AND ADDRESSES
Benedict College
Office of Research
1600 Harden St.
Columbia, SC   29204 -1058

8. PERFORMING ORGANIZATION REPORT NUMBER

9. SPONSORING/MONITORING AGENCY NAME(S) AND ADDRESS (ES)
U.S. Army Research Office
P.O. Box 12211
Research Triangle Park, NC 27709-2211

10. SPONSOR/MONITOR'S ACRONYM(S)
ARO

11. SPONSOR/MONITOR'S REPORT NUMBER(S)
62613-EL-H.12

12. DISTRIBUTION AVAILIBILITY STATEMENT
Approved for Public Release; Distribution Unlimited

13. SUPPLEMENTARY NOTES
The views, opinions and/or findings contained in this report are those of the author(s) and should not contrued as an official Department of the Army position, policy or decision, unless so designated by other documentation.

14. ABSTRACT
Using theoretical and computational chemistry methods, we have studied the oxygen reduction and proton transfer in molten carbonate salts related to solid oxide fuel cells, and adsorption of nerve agents of sarin on surfaces of CaO, graphene and graphane. The mechanism of oxygen reduction through CO_5^{2-} and CO_4^{2-} is confirmed for the first time by DFT. It was found the proton has very good mobility in molten carbonate salts with activation energy of ~8.0 kcal/mol, which agrees with the value measured by experiment. For sarin on the selected surfaces, its polarized phosphate region as Lewis base acts as the binding agent. The binding energy ranges from 2.4-13.2

15. SUBJECT TERMS
Oxygen reduction, proton transfer, ab initio calculations, nerve agent, adsorption, electron transfer

16. SECURITY CLASSIFICATION OF:			17. LIMITATION OF ABSTRACT	15. NUMBER OF PAGES	19a. NAME OF RESPONSIBLE PERSON
a. REPORT	b. ABSTRACT	c. THIS PAGE	UU		Changyong Qin
UU	UU	UU			19b. TELEPHONE NUMBER
					803-705-4582

Report Title

Final Report: Theoretical Studies of Oxygen Reduction and Proton Transfer in SOFCs and Nerve Agents on Selected Surfaces

ABSTRACT

Using theoretical and computational chemistry methods, we have studied the oxygen reduction and proton transfer in molten carbonate salts related to solid oxide fuel cells, and adsorption of nerve agents of sarin on surfaces of CaO, graphene and graphane. The mechanism of oxygen reduction through CO_5^{2-} and CO_4^{2-} is confirmed for the first time by DFT. It was found the proton has very good mobility in molten carbonate salts with activation energy of ~8.0 kcal/mol, which agrees with the value measured by experiment. For sarin on the selected surfaces, its polarized phosphate region as Lewis-base acts as the binding agent. The binding energy ranges from 2.4-13.2 kcal/mol at the level of CI, showing relative weak interactions with the surfaces.

Enter List of papers submitted or published that acknowledge ARO support from the start of the project to the date of this printing. List the papers, including journal references, in the following categories:

(a) Papers published in peer-reviewed journals (N/A for none)

Received   Paper

01/23/2015 6.00 Y. Gong, X. Li, L. Zhang, W. Tharp, C. Qin, K. Huang. Molten Carbonates as an Effective Oxygen
Reduction Catalyst for 550-650 C Solid Oxide Fuel Cells,
Journal of the Electrochemical Society, (06 2013): 958. doi: 10.1149/2.031309jes

01/23/2015 4.00 Ioannis D. Petsalakis, Giannoula Theodorakopoulos, Jerry Whitten. Electronic structure and spectra of
$(Cu_2O)_n-H_2O$ Complexes,
Phys. Chem. Chem. Phys., (11 2014): 428. doi: 10.1039/C4CP04303K

01/23/2015 5.00 L. Zhang, W. Tharp, C. Qin, K. Huang, X. Li, Y. Gong. Promoting Electrocatalytic Activity of a Composite
SOFC Cathode La0.8Sr0.2MnO3+ /Ce0.8Gd0.2O2- with Molten Carbonates,
Journal of the Electrochemical Society, (12 2013): 226. doi: 10.1149/2.034403jes

01/23/2015 7.00 Brian N. Papas, Ioannis D. Petsalakis, Giannoula Theodorakopoulos, Jerry L. Whitten. CI and DFT
Studies of the Adsorption of the Nerve Agent Sarin on Surfaces,
The Journal of Physical Chemistry C, (10 2014): 23042. doi: 10.1021/jp505258k

11/19/2015 9.00 Xueling Lei, Kahla Haines, Kevin Huang, Changyong Qin. DFT Study of Oxygen Dissociation in Molten
Carbonate,
The Journal of Physical Chemistry A, (08 2015): 0. doi: 10.1021/acs.jpca.5b06527

TOTAL: **5**

Number of Papers published in peer-reviewed journals:

(b) Papers published in non-peer-reviewed journals (N/A for none)

<u>Received</u>   <u>Paper</u>

   TOTAL:

Number of Papers published in non peer-reviewed journals:

(c) Presentations

Number of Presentations: 0.00

Non Peer-Reviewed Conference Proceeding publications (other than abstracts):

<u>Received</u>   <u>Paper</u>

   TOTAL:

Number of Non Peer-Reviewed Conference Proceeding publications (other than abstracts):

Peer-Reviewed Conference Proceeding publications (other than abstracts):

<u>Received</u>   <u>Paper</u>

   TOTAL:

Number of Peer-Reviewed Conference Proceeding publications (other than abstracts):

(d) Manuscripts

<u>Received</u>   <u>Paper</u>

11/19/2015 10.00 Xueling Lei, Changyong Qin, Kevin Huang. Kinetics and Mechanism of Proton Transfer in Molten Lithium
Carbonate: Insights from Static and Dynamic DFT Studies ,
Angew Chem Int Ed Engl (11 2015)

     TOTAL: **1**

Number of Manuscripts:

Books

<u>Received</u>   <u>Book</u>

     TOTAL:

<u>Received</u>   <u>Book Chapter</u>

     TOTAL:

Patents Submitted

Patents Awarded

Awards

Kahla Haines, 2nd place, Benedict College Summer research institute
Changyong Qin, Distinguished Faculty of Benedict College 2013
Changyong Qin, Excellence in Teaching Award by SCICU 2014

Graduate Students

NAME	PERCENT_SUPPORTED
FTE Equivalent:	
Total Number:	

Names of Post Doctorates

NAME	PERCENT_SUPPORTED
Brian Papas	1.00
FTE Equivalent:	**1.00**
Total Number:	**1**

Names of Faculty Supported

NAME	PERCENT_SUPPORTED	National Academy Member
Changyong Qin	0.25	
FTE Equivalent:	**0.25**	
Total Number:	**1**	

Names of Under Graduate students supported

NAME	PERCENT_SUPPORTED	Discipline
Kahla Haines	0.25	
FTE Equivalent:	**0.25**	
Total Number:	**1**	

Student Metrics
This section only applies to graduating undergraduates supported by this agreement in this reporting period

The number of undergraduates funded by this agreement who graduated during this period: 1.00

The number of undergraduates funded by this agreement who graduated during this period with a degree in science, mathematics, engineering, or technology fields:...... 1.00

The number of undergraduates funded by your agreement who graduated during this period and will continue to pursue a graduate or Ph.D. degree in science, mathematics, engineering, or technology fields:...... 0.00

Number of graduating undergraduates who achieved a 3.5 GPA to 4.0 (4.0 max scale):...... 1.00

Number of graduating undergraduates funded by a DoD funded Center of Excellence grant for Education, Research and Engineering:...... 0.00

The number of undergraduates funded by your agreement who graduated during this period and intend to work for the Department of Defense 0.00

The number of undergraduates funded by your agreement who graduated during this period and will receive scholarships or fellowships for further studies in science, mathematics, engineering or technology fields:...... 0.00

Names of Personnel receiving masters degrees

NAME

Total Number:

Names of personnel receiving PHDs

NAME

Total Number:

Names of other research staff

NAME   PERCENT_SUPPORTED

FTE Equivalent:
Total Number:

Sub Contractors (DD882)

Inventions (DD882)

Scientific Progress

See the technical reports attached.

Technology Transfer

NONE

Theoretical Studies of Oxygen Reduction and Proton Transfer in SOFCs and Nerve Agents on Selected Surfaces

Changyong Qin, Benedict College, Columbia, SC 29204 (PI)

PART A: Oxygen Reduction in SOFCs

I. Computational Methods

All calculations were performed in Gaussian09 suite of quantum programs. Local minimum structures were optimized using the generalized gradient approximation (GGA) based hybrid functional of b3lyp combining with the all-electron basis sets and polarization functions of 6-31G(d). The vibrational frequencies were calculated at the same theoretical level, ensuring that the reactant and product structures are located at a true minimum on the potential energy surface (PES) and the transition state is a first order saddle point on PES as well. The atomic polar tensor (APT) charges were computed through frequency calculations. All resulting energies include the zero-point energy (ZPE) corrections. In addition, variable basis sets and methods were applied to verify the accuracy and reliability of the B3LYP/6-31G(d) method, including 6-311G++(d), CBSB7, LANL2DZ, MP4 and CCSD(T).
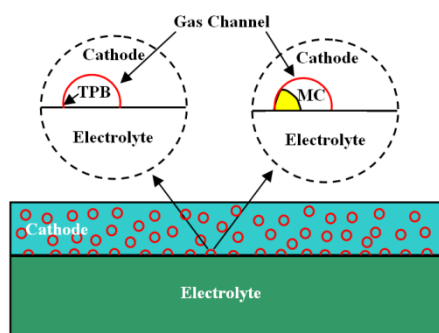

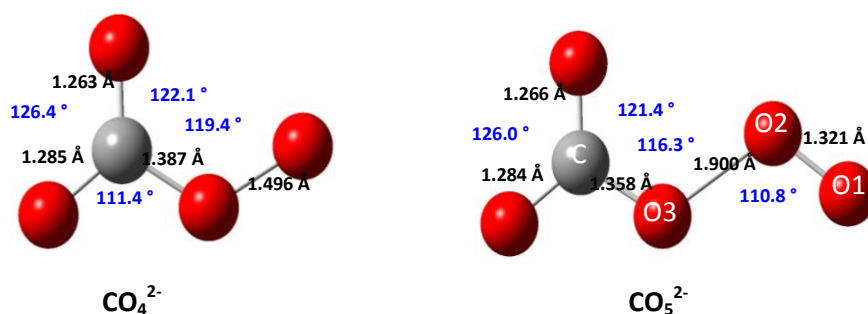**Figure 1: Illustration of Oxygen Reduction in SOFCs (Left: No MC, Right: With MC).**

Figure 2: Optimized structures of CO_4^{2-} and CO_5^{2-} at the B3LYP/6-31G (d) level.

II. Results and Discussions

2.1 Structure of CO_4^{2-}, CO_5^{2-} and carbonate clusters

The structures of CO_4^{2-} and CO_5^{2-} were optimized at the B3LYP/6-31G(d) level, as displayed in Fig. 2. The calculated bond lengths and bond angles in both CO_4^{2-} and CO_5^{2-} are in excellent agreement with the previous reported values. To test the reliability of B3LYP, we re-optimized the structure of CO_5^{2-} using MP2 with the same basis set. All structural parameters are listed in Table 1. The difference between the results from two methods ranges 0.4-2.9%, showing very good agreement. On the other hand, the energy change for $CO_3^{2-}+O_2 \rightarrow CO_5^{2-}$ is calculated to be -105.5 kJ/mol and -87.3 kJ/mol by B3LYP and CCSD(T), respectively. Similarly, the formation energy of CO_4^{2-} ($CO_3^{2-}+1/2O_2 \rightarrow CO_4^{2-}$) is -9.8 kJ/mol and -5.4 kJ/mol by B3LYP and CCSD(T), respectively. All testing results have convinced the reliability of B3LYP in treating molten carbonate systems.

Table 1 The structural parameters of CO_5^{2-} obtained from B3LYP and MP2 (Distance in angstroms, and angle in degrees).

	O1-O2	O2-O3	O3-C	O1-O2-O3	O2-O3-C
MP2	1.316	1.957	1.380	110.4	114.2
B3LYP	1.321	1.900	1.358	110.8	116.3
Diff.%	0.4%	2.9%	1.6%	0.4%	1.7%

Fig. 3 shows the optimized structures of $(Li_2CO_3)_4$, $(Na_2CO_3)_4$, and $(K_2CO_3)_4$ at the b3lyp/6-31g(d) level. As seen from each picture, each alkali metal atom (M) is bonded to three carbonate oxygen atoms, while each carbonate oxygen atom is connected to two M atoms. This configuration is same as those in their crystal structures of bulk Li_2CO_3, Na_2CO_3, and K_2CO_3. In addition, the average bond length between alkali metal atom and oxygen (d_{M-O}) in $(Li_2CO_3)_4$, $(Na_2CO_3)_4$ and $(K_2CO_3)_4$ is calculated to be 1.968 Å, 2.305 Å and 2.666 Å, respectively, which agrees well with experimental values of 1.960 Å, 2.377 Å and 2.870 Å, respectively. Our recent *ab initio* molecular dynamics (AIMD) study confirms that the volume expansion of Li_2CO_3 is only 3% at the temperature of 1300 K (Calculated melting point ~1000 K), implying that the Li-O bond distance will not change significantly in the molten lithium carbonate. All evidences above give us confidence in using $(M_2CO_3)_4$ to describe the structure of molten carbonates. More importantly, such cluster models are more affordable when treating such large molecular systems.

$(Li_2CO_3)_4$ $(Na_2CO_3)_4$ $(K_2CO_3)_4$

**Figure 3: Optimized structures of $(M_2CO_3)_4$ (M=Li, Na, K) at the B3LYP/6-31G (d) level.**

2.2 Oxygen dissociation in the (Li₂CO₃)₄ cluster

Fig. 4 shows the structural evolution of oxygen, the beginning, transitioning and ending states, in the process of dissociation in a lithium carbonate cluster together with the energy profile. As seen from Fig. 4 (a), the inserted figure is the structure with minimum energy optimized from the $(Li_2CO_3)_4O_2$ cluster. It is found that the added oxygen molecule bonds with one carbonate anion to form CO_5^{2-}, which is circled by green dashed line. The existence of CO_5^{2-} in lithium carbonate agrees with the previous assumption and proves that oxygen is captured by carbonate ions in MC. From the amplified figure, the bond distance of O25-O26 is 1.427 Å, which is 0.106 Å longer than that of the free CO_5^{2-} in the gas phase (Fig. 2). However, the O26-O10 bond is 1.474 Å only and 0.426 Å shorter than in the single CO_5^{2-}. The APT charge of O25 and O26 is calculated to be 0.09e and -0.69e, respectively. The negative charge is approximately 75% from O10 and 25% from surrounding Li atoms. Because O26 is the end oxygen and connected to three Li atoms, it is not surprising that the electron will be pulled towards O26 by Coulomb force. The electron density is likely injected into the anti-bonding orbital of O25-O26, causing the increase of the bond distance. Both calculated bond distances and charges indicate that the $O_2-CO_3^{2-}$ interaction is of covalent bonding and the oxygen molecule is weakened by binding to carbonate ion.

(a) Reactant

(b) TS

(c) Product

(d) Energy Barrier
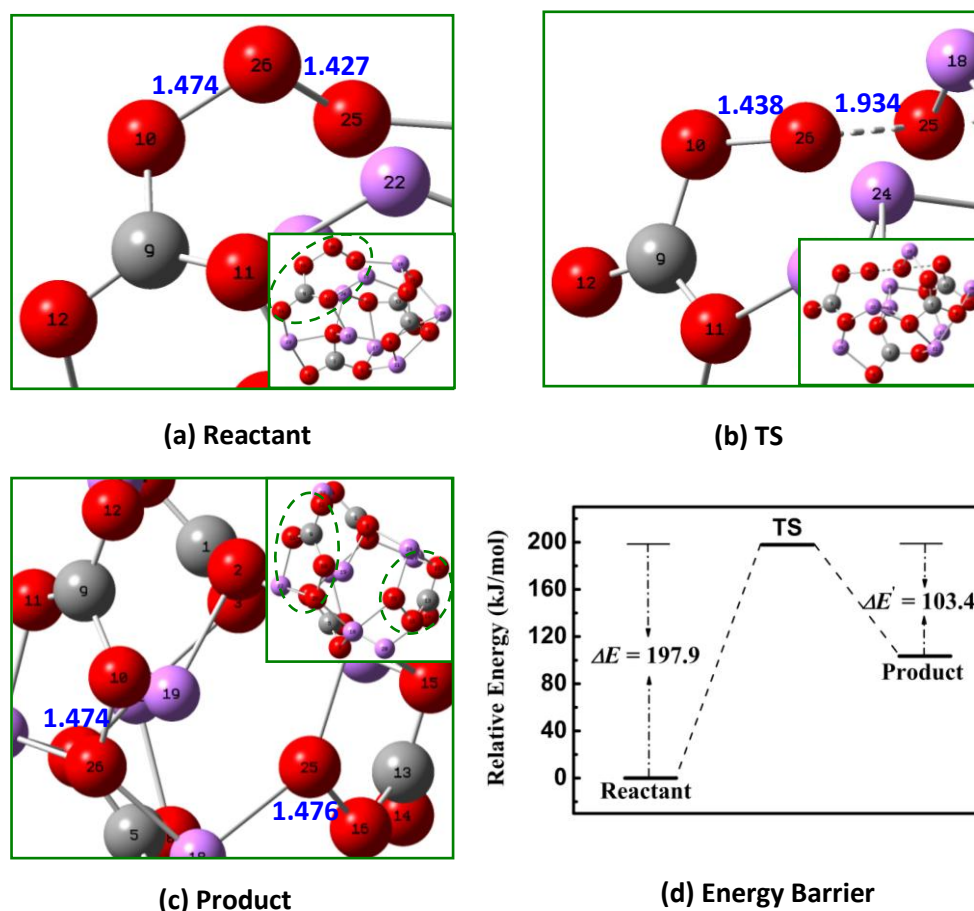
Figure 4: Structures of beginning, transitioning and ending state in (Li₂CO₃)₄O₂ as well as PES. (Distance in Å; gray, red, and purple ball represents C, O, and Li, respectively.)

    As O25 leaves O26 and moves towards another carbonate oxygen atom O16. A new O25-O16 bond is forming while O25-O26 is breaking. This leads to a transition state (TS) located on the PES (Fig. 3b). At TS, the distance between O25 and O26 is enlarged to 1.934 Å, while the distance between O10 and O26 is 0.036 Å shorter. During this process, the system experiences an energy barrier of 197.9 kJ/mol. Finally, O25-O26 bond is completely broken with a distance of ~3.0 Å, and O25-O16 bond is formed. The PES calculated by intrinsic reaction coordinate (IRC) connects the starting structure with CO_5^{2-}, the TS and the final structure with two CO_4^{2-} (Fig. 3c). This gives a full picture of oxygen dissociation in lithium carbonate. Obviously, with the aid of carbonate, oxygen dissociation is facilitated.
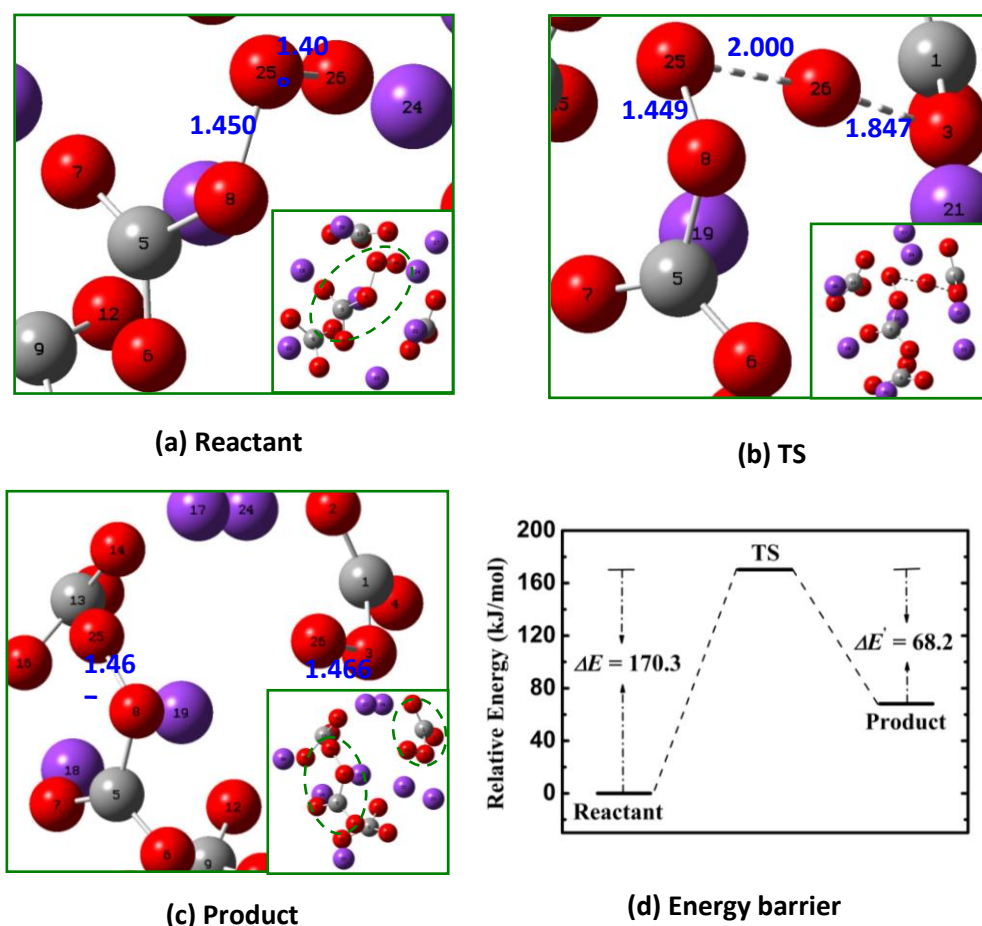

(a) Reactant

(b) TS

(c) Product

(d) Energy Barrier
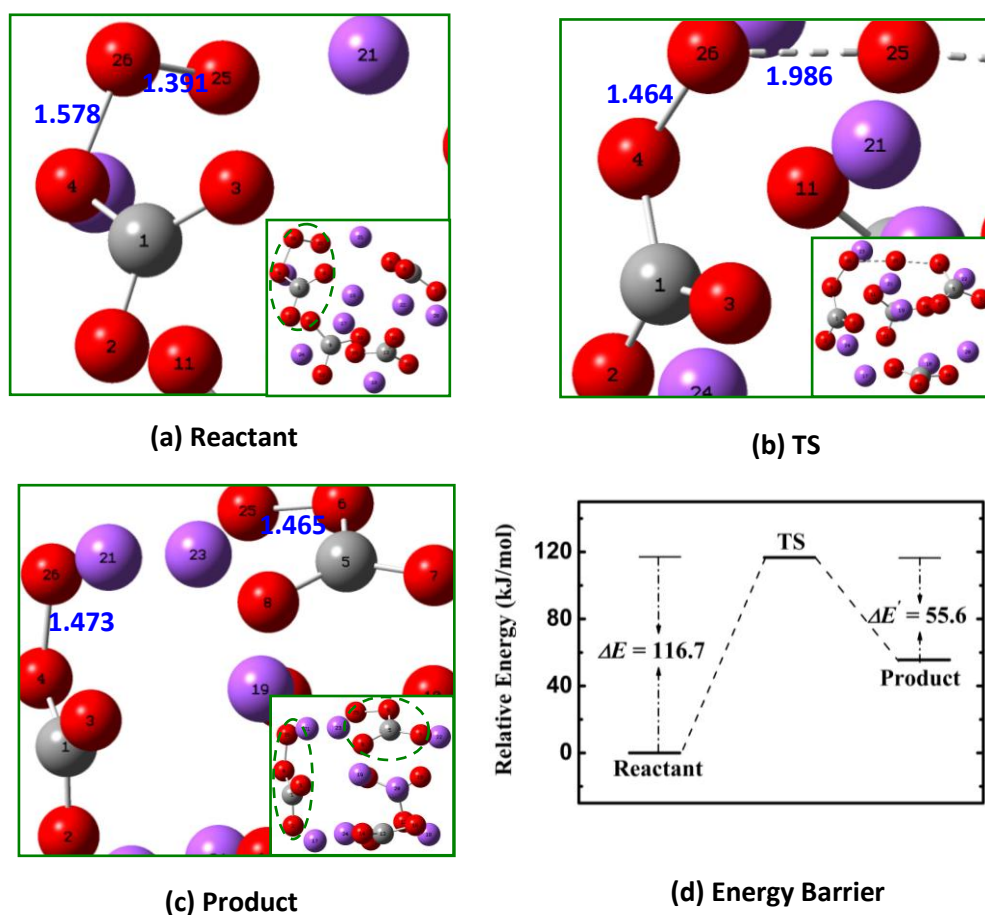
Figure 5: Structures of beginning, transitioning and ending state in $(Na_2CO_3)_4O_2$ as well as PES. (Distance in Å; gray, red, and purple ball represents C, O, and Na, respectively.)

2.3 Oxygen dissociation in the $(Na_2CO_3)_4$ cluster

    Fig. 5 shows the structures of the beginning, transitioning and ending states for oxygen dissociation in a sodium carbonate cluster as well as the energy profile. Similarly, the oxygen molecule of O25-O26 was introduced to the $(Na_2CO_3)_4$ cluster and a bond was formed between O26 and O4. The formed local structure is also CO_5^{2-} same as in $(Li_2CO_3)_4$ (green dashed line in

the insert figure). The bond length of O4-O26 and O25-O26 is 1.578 Å and 1.391 Å, respectively. The APT charge of O25 and O26 is calculated to be 0.21e and -0.60e, respectively. As seen from Fig. 4 (b), O25 moves away from O26 towards O6, initiating a dissociation process. At TS, the distance of O25-O26 is significantly elongated to 1.986 Å and the O4-O26 bond length is slightly shortened by 0.114 Å. At the end, O25 bonds with O6 to form CO_4^{2-}, and the oxygen dissociation is completed. The calculated PES indicates that the oxygen dissociation reaction has an energy barrier of 116.7 kJ/mol.

(a) Reactant

(b) TS

(c) Product

(d) Energy barrier

Figure 6: Structures of beginning, transitioning and ending state in $(K_2CO_3)_4O_2$ as well as PES. (Distance in Å; gray, red, and purple ball represents C, O, and K, respectively.)

2.4 Oxygen dissociation in the $(K_2CO_3)_4$ cluster

Fig. 6 shows the structural features of the beginning, transitioning and ending states for oxygen dissociation in a potassium carbonate cluster as well as the energy profile. Similarly, O25-O26 is bonded to O8 as a diatomic oxygen. The O8-O25 and O25-O26 bond length is calculated to be 1.450 Å and 1.408 Å, respectively. The APT charge on O25 and O26 is 0.11e and -0.69 e, respectively. As O26 moves away from O25 towards to O3, the O25-O26 bond

starts breaking, while O3-O26 bond starts forming. At TS, O25-O26 reaches a distance of 2.000 Å. The calculated energy barrier for the oxygen dissociation is 170.3 kJ/mol. Finally, the oxygen dissociation is finished as the O26-O3 bond is shortened to 1.466 Å and O25-O26 elongated to 3.470 Å. The reaction path on PES was verified by IRC calculations.

2.5 Mechanism of Oxygen Reduction by MC in SOFCs

For the reaction of oxygen reduction (ORR) in SOFCs, the adsorption and dissociation of oxygen on the surface of cathode is of great importance. Without MC, the reaction proceeds through superoxide and peroxide intermediates on the surface of solid oxide cathode [37]. The adsorption of oxygen on the ionic solid surface is limited to the surface defect sites only. With the presence of MC, the formation of CO_5^{2-} was confirmed in three alkali molten carbonates, indicating a chemisorption of gas oxygen on the surface of MC modified cathode. The binding energy was estimated to be 101.7 kJ/mol. The strong interaction of oxygen with MC implies a facilitated ORR process with the aid of MC on the cathode of SOFCs.

Once CO_5^{2-} is formed, the next step is to react with another CO_3^{2-} to form two CO_4^{2-}. This step is rate-limiting on PES (Fig. 7). The calculated energy barrier is 197.9, 116.7, and 170.3 kJ/mol for lithium, sodium and potassium molten salt, respectively. The energy change for this step is calculated to be +103.3, +55.6 and +68.2 kJ/mol, respectively. This fairly agrees with the calculated value of +86.2 kJ/mol for $CO_5^{2-} + CO_3^{2-} \rightarrow 2CO_4^{2-}$ in gas phase at the B3LYP/6-31G(d) level. Surprisingly, it was found that sodium carbonate has the lowest activation energy and also smallest energy change for oxygen dissociation. This agrees with the experimental observations that the cathodes modified by Li_2CO_3-Na_2CO_3 (52:48 mol %) in SOFCs have a better performance than those by Li_2CO_3-K_2CO_3 (62:38 mol %) [38]. Table 2 gives the bond distance of C-O and M-O in the selected carbonates, the C-O bond is almost same in all three salts, but the M-O bond distance increases from Li, Na to K due to the change of atomic size. The APT charge on Li, Na and K is calculated to be 0.751 e, 0.769 e and 0.840 e, respectively, showing good consistency with the electronegativity. The electrostatic potential energy is described by Q/d_{M-O}, and the calculated value is 0.382 e/Å, 0.334 e/Å and 0.315 e/Å, respectively. Lower potential energy and lighter the ions, the impendence for the movement of ions in MC will be lower and so the energy barrier be for oxygen dissociation and diffusion in MC. This can partially explain the lower energy barrier in sodium carbonate than the other two salts. However, more details based on MD simulations will be reported in near future.

Table 2 Selected bond distances (d_{C-O} and d_{M-O}), APT charges (Q_M), and electrostatic potentials (Q/d_{M-O}).

Clusters	d_{C-O}	d_{M-O}	Q_M	Q/d_{M-O}
$(Li_2CO_3)_4O_2$	1.299	1.968	0.751	0.382
$(Na_2CO_3)_4O_2$	1.299	2.305	0.769	0.334
$(K_2CO_3)_4O_2$	1.302	2.666	0.840	0.315

* Bond distance in Å and charge in e, all values are average.

If the reaction is approximated as Eqn. 5, then $CO_5{}^{2-}$ can be treated as an intermediate and the steady-state theory can be applied. The reaction rate is described by Eqn. 6. The effective activation energy for the overall reaction is estimated to be 96.2, 15.1, and 68.6 kJ/mol in lithium, sodium and potassium molten carbonate, respectively. The pseudo one-step reaction is exothermic and favored by chemical thermodynamics for Na and K, but slightly endothermic for Li. From the view of chemical kinetics, lithium carbonate is not a favorable molten salt for ORR, but lithium carbonate can significantly reduce the melting point of sodium and potassium carbonates when eutectic ratios are adopted. In Eqn. 6, the concentration of $CO_3{}^{2-}$ is a constant, therefore the reaction rate is solely determined by the pressure of oxygen. Increasing the oxygen pressure will improve the kinetics of the cathode in SOFCs.

$$2CO_3^{2-} + O_2 \underset{k_{-1}}{\overset{k_1}{\longleftrightarrow}} CO_5^{2-} + CO_3^{2-} \overset{k_2}{\longrightarrow} 2CO_4^{2-} \qquad (5)$$
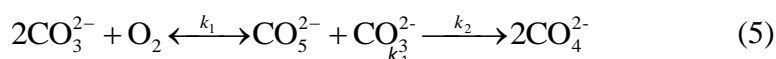
$$\text{Reaction Rate} = \frac{k_1}{k_{-1} + k_2}[O_2][CO_3^{2-}]^2 \qquad (6)$$

Given that O1-O2-O3 in $CO_5{}^{2-}$ (Fig. 1) is ozone-like and possibly has considerable biradical character, it is necessary to verify the reliability of B3LYP in this study. Previous studies by Gerber and co-workers on Criegee Intermediates (CIs) have proven that MP4 and CCSD(T) are reasonably reliable in treating such molecular systems. Therefore, we have calculated single point energies using variable basis sets and methods. Calculated energy barriers for oxygen dissociation are summarized in Table 3. Only small changes occur when the basis set is changed from 6-31G(d), 6-311G++(d) to CBSB7, all using B3LYP. Considering the computing cost with MP4 and CCSD(T), we had to decrease the basis set to LANL2DZ. The use of effective core potentials (ECPs) has largely reduced the computing time. The calculated energy barriers by MP4 are higher than those by B3LYP, about 10% in $(K_2CO_3)_4$ and 17% in $(Na_2CO_3)_4$, but only 1% in $(Li_2CO_3)_4$. However, an excellent agreement was observed between B3LYP and CCSD(T). The comparative results have verified that the results by the B3LYP/6-31G(d) method for the oxygen dissociation in $(M_2CO_3)_4$ (M=Li, Na, K) clusters are accurate and the method is reliable for similar studies in future.
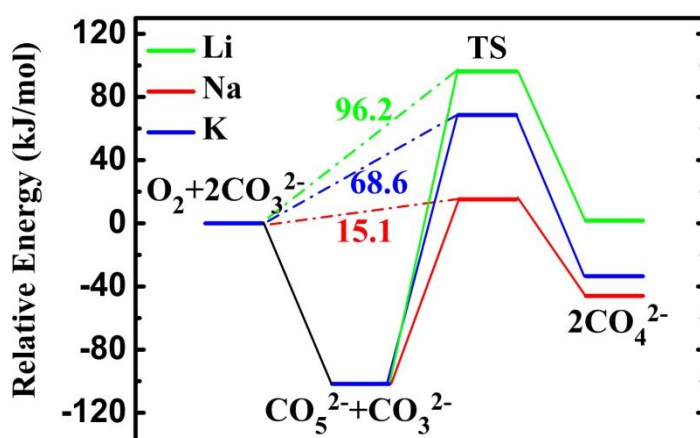

Figure 7: PES of Oxygen Dissociation in the $(M_2CO_3)_4$ clusters, M=Li, Na, and K.

Table 3 The activation energy (kJ/mol) of oxygen dissociation in $(M_2CO_3)_4$ (M=Li, Na, K).

	B3LYP/6-31G(d)	B3LYP/6-311++G(d)	B3LYP/CBSB7
$(Li_2CO_3)_4$	204.2/197.9(ZPE)	198.7	197.5
$(Na_2CO_3)_4$	115.9/116.7(ZPE)	115.9	115.1
$(K_2CO_3)_4$	171.1/170.3(ZPE)	159.8	159.4

	B3LYP/LANL2DZ CCSD(T)/LANL2DZ		MP4/LANL2DZ
$(Li_2CO_3)_4$	197.1	199.6	194.6
$(Na_2CO_3)_4$	87.9	103.3	95.4
$(K_2CO_3)_4$	141.0	154.0	146.0

III. Summary of Part A

We have reported a DFT study of oxygen dissociation process in selected molten carbonates. It was found that the adsorption of oxygen to molten carbonate is of chemical type, and leads to the formation of CO_5^{2-} in MC, which was confirmed for the first time by DFT calculations. The energy barrier for its dissociation is calculated to be 197.9, 116.7, and 170.3 kJ/mol at the B3LYP/6-31G(d) level in the $(M_2CO_3)_4$ cluster, M = Li, Na, and K, respectively. If the reaction of $O_2 + 2CO_3^{2-} \rightarrow 2CO_4^{2-}$ is approximated as a one-step reaction, the activation energy is estimated to be 96.2, 15.1, and 68.6 kJ/mol, respectively. The reaction rate is the first order to the pressure of oxygen. To our surprise, sodium carbonate has the lowest energy barrier for oxygen dissociation in molten sodium carbonate, which is consistent to the recent experimental findings. It is very clear that the molten carbonate salt has directly participated in the ORR process and plays an important role as a catalyst. The oxygen reduction has been facilitated by MC and enhanced cell performance has been observed. In addition, the B3LYP/6-31G(d) method is verified to be accurate and reliable in treating such molten carbonate salt systems.

Theoretical Studies of Oxygen Reduction and Proton Transfer in SOFCs and Nerve Agents on Selected Surfaces

Changyong Qin, Benedict College, Columbia, SC 29204 (PI)

PART B: Mechanism of Proton Transfer in SOFCs

I. Computational Methods

1.1 Static DFT Calculations in Gaussian 09

Static DFT calculations were carried out at the B3LYP/6-31G(d,p) level as implemented in the Gaussian 09 package. Geometries of ground-state and transition state (TS) of $[(Li_2CO_3)_8H]^+$ clusters were fully optimized. To confirm each optimized stationary point, the vibrational frequencies were examined at the same theoretical level, ensuring that the reactant and product structures are local minimum while the transition state is a first order saddle point on the potential energy surface (PES). To quickly and correctly search out the TS, we first performed the SCAN calculations and then performed TS calculations using the geometry with the highest energy . Finally, the intrinsic reaction coordinate (IRC) calculations were carried out to judge the reaction direction.

1.2 Dynamic DFT Calculations in VASP

Using VASP 5.3 package, first-principles molecular dynamics (FPMD) calculations were performed. The structure of $[(Li_2CO_3)_8H]^+$ cluster optimized at the B3LYP/6-31G(d,p) level was used as the initial structure of FPMD simulations. All FPMD simulations were conducted with the NVT canonical ensemble. PAW-PBE potentials supplied with the VASP package were used for H (ultrasoft), Li (s1p0), C (s2p2), and O (s2p4). The Verlet algorithm was integrated with Newton's equations of motion at a time step of 2 fs for a total simulation time of 6 ps, *i.e.*, 3000 steps. The frequency of the temperature oscillations was controlled by the Nosé mass during the simulations. Energy cutoff of 500 eV and a $1\times1\times1$ k-point mesh were used.

For the simulations of proton transfer in the bulk lithium molten carbonate, the supercell of $1\times2\times2$ was first melted by virtually heated to 3000 K within the NVT ensemble. Then, a melt configuration was randomly chosen to test the optimal lattice constant while considering the change in system volume induced by the phase transition. Then, the melt configuration was subjected to a cooling process at a rate of 2.67×10^{13} K/s to obtain a molten carbonate structure at 1100 K, 1200 K, and 1300 K. Finally, we randomly put the proton in the lithium molten carbonate and simulated for another 6 ps at the temperatures of 1100 K, 1200 K, and 1300 K, respectively.

II. Results and Discussion

2.1 Intramolecular Transfer of Proton in the Carbonate Ion

First, we studied the proton migration in intra-$(CO_3)^{2-}$ ion. As shown in Fig.1, during the transfer, the bond between O1 and H^+ is first broken, followed by H^+ moving toward the mirror position between O1 and O2, namely the TS. The bond between O2 and H^+ is then formed, completing the H^+-transfer. We find that the energy barrier for H^+-transfer between O1 and O2 is 22.3

kcal/mol. In addition, to test the reliability of B3LYP, the CCSD(T) method with the same basis set was used to compute the single point energies. The activation energy computed at CCSD(T)/6-31G (d,p) level is 25.5 kcal/mol, which is only slightly higher than that obtained from B3LYP/6-31G (d,p), about 3.2 kcal/mol. The comparative activation energy has convinced the B3LYP method is reliable in treating such systems.
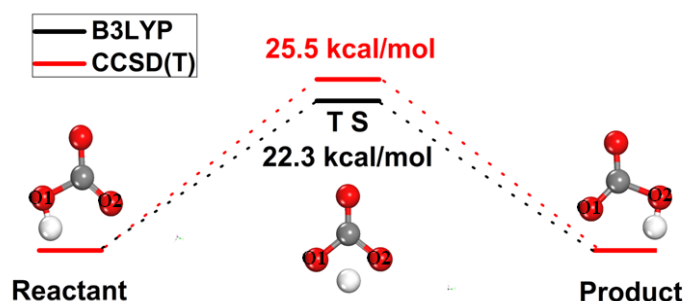
Fig. 1 The structures of reactant, transition state (TS), and product as well as the relative energy for proton transfer in intra-$(CO_3)^{2-}$ ion. The proton, carbon, and oxygen atoms are shown as white, gray, and red balls, respectively.

Second, we studied the proton transfer in intra-carbonate and inter-carbonate in $(Li_2CO_3)_8$ cluster. Fig. 2(a) and Fig. 2(b) indicates the proton transfer in intra-carbonate on the surface of $(Li_2CO_3)_8$ cluster and inside the $(Li_2CO_3)_8$ cluster, respectively. As seen from Fig. 2, both migrations experience the H^+-O bond broken and reforming, and the energy barriers are 46.8 kcal/mol and 49.0 kcal/mol, respectively.
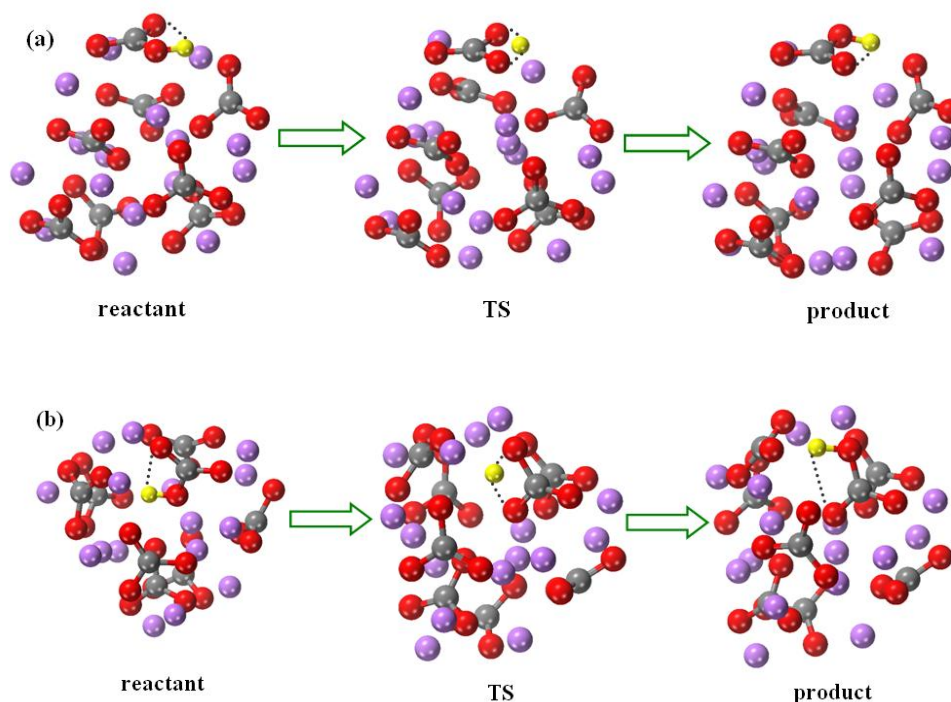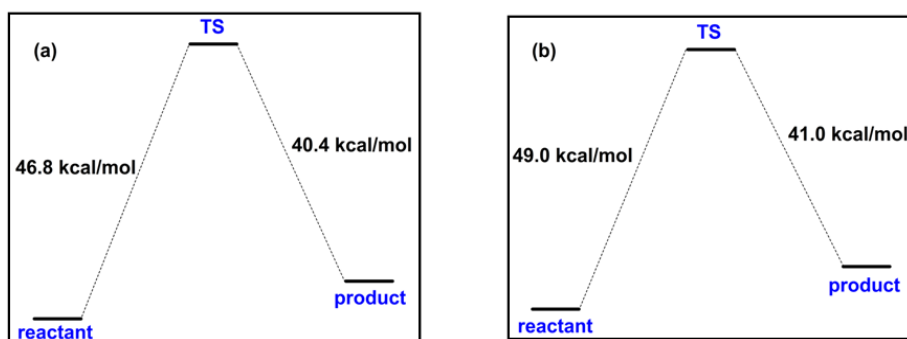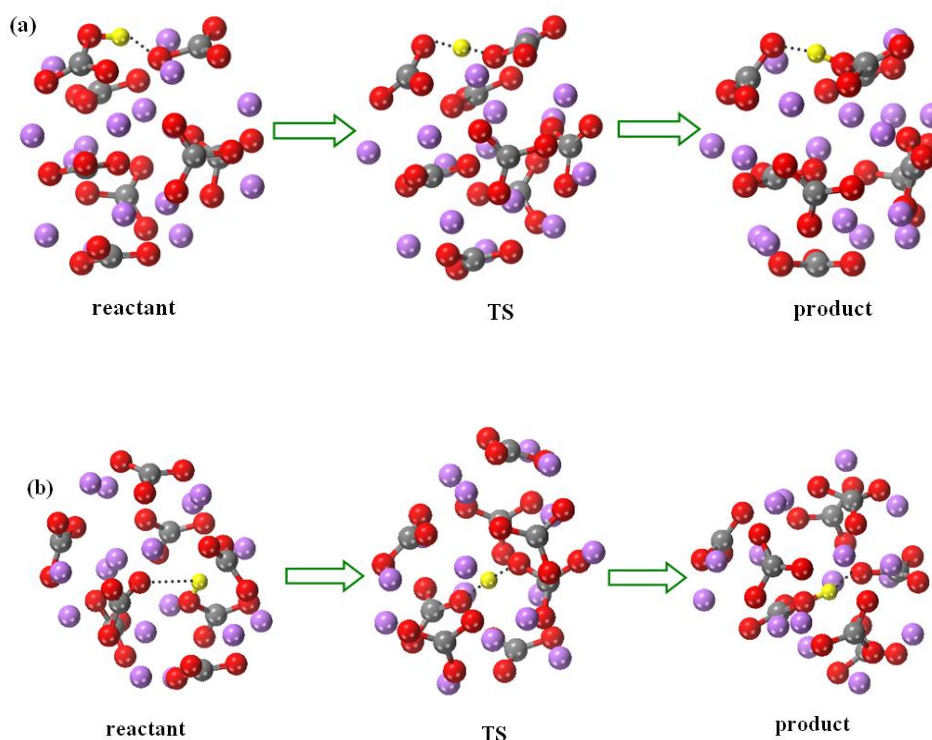
Fig. 2 The structures of reactant, transition state (TS), and product as well as the relative energy for proton migration in intra-carbonate in the $(Li_2CO_3)_8$ cluster. The proton, carbon, oxygen and lithium atoms are shown as yellow, gray, red, and purple respectively.

2.1 Intermolecular Transfer of Proton between Carbonate Ions

Fig. 3(a) and Fig. 3(b) indicates the proton transfer in inter-carbonate on the surface of $(Li_2CO_3)_8$ cluster and inside the $(Li_2CO_3)_8$ cluster, respectively. As seen from Fig. 3, unlike proton transfer in intra-carbonate as shown in Fig.2, although migrations of proton transfer in inter-carbonate experience the H^+-O bond broken and reforming, but the energy barriers are decreased to 1.1 kcal/mol and 7.7 kcal/mol, respectively. This is not surprising because when the proton transfers between carbonate ions (inter-carbonate), each carbonate ion can adjust its position accordingly, decreasing the energy barrier of H^+-transfer.
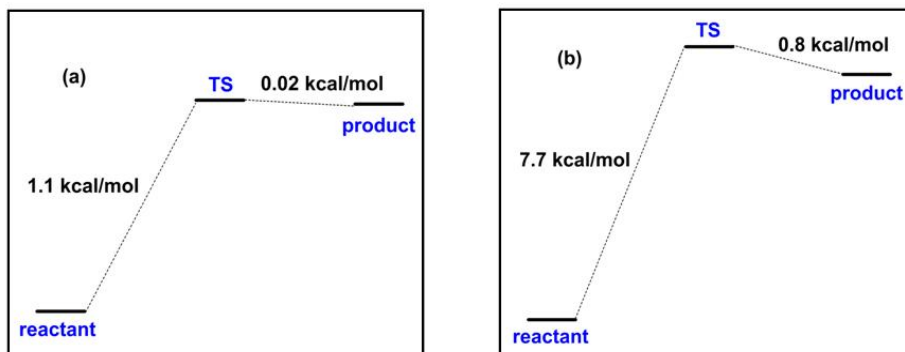
Fig. 3 The structures of reactant, transition state (TS), and product as well as the relative energy for proton migration in inter-carbonate in the $(Li_2CO_3)_8$ cluster. The proton, carbon, oxygen and lithium atoms are shown as yellow, gray, red, and purple respectively.

Apparently, comparison of the above energy barrier suggests that there are no energetics difference for proton transfer on the surface of $(Li_2CO_3)_8$ cluster and inside the $(Li_2CO_3)_8$ cluster, and the proton transfer prefers inter-carbonate to intra-carbonate in the $(Li_2CO_3)_8$ cluster

### 2.3 Dynamic DFT on Proton Transfer in $(Li_2CO_3)_8$

To simulate the proton migration features in real molten carbonate at finite temperatures, we carried out the first-principles molecular dynamics (FPMD) calculations. Fig. 4 shows the trajectories of proton, selected carbon and oxygen atom in the $(Li_2CO_3)_8$ cluster simulated at 1100 K, 1200 K, and 1300 K for 6 ps. We can see that the trajectory of proton is very dispersed while the trajectory of carbon is very localized, which indicates that the proton transfer in the $(Li_2CO_3)_8$ cluster is quite fast with large displacement, but the carbon atom only vibrates at its original site and unsuccessful jumps with much limited displacement. It should be noted that the trajectory of selected oxygen atom is dispersed somewhat, indicating that the oxygen atom adjust its position by rotation or rolling during the proton transfer in inter-carbonate in the $(Li_2CO_3)_8$ cluster.

The mean square displacement (MSD) is determined by the ensemble average:

$$\text{MSD} = <\delta r^2> = \frac{1}{N}\frac{1}{n}\sum_{i=0}^{n}\sum_{m=0}^{N}[r_m(t+t_{0i}) - r_m(t_{0i})]^2 \qquad (1),$$

where N is the number of ions in the system, n is the number of time origins, t is the time, and t_{0i} is the initial timestep originating at time i. In this work, at least three FPMD running were conducted for the same structure at each temperature, aiming to obtain an averaged MSD for accuracy. The diffusion coefficient is calculated by fitting the slope of the MSD vs. time. To obtain a rational diffusion coefficient, only the second half MSD data are included in the linear fitting. Fig. 5 shows the calculated mean square displacement for proton transfer in the $(Li_2CO_3)_8$ cluster simulated at the temperature of 1100 K, 1200 K, and 1300 K for 6 ps. Evidently, the MSD of proton increases linearly with time, indicating a fast proton migration. Moreover, the slope of MSD increases as the temperature increases, indicating the ability of proton diffusion

increases with the temperature increasing.
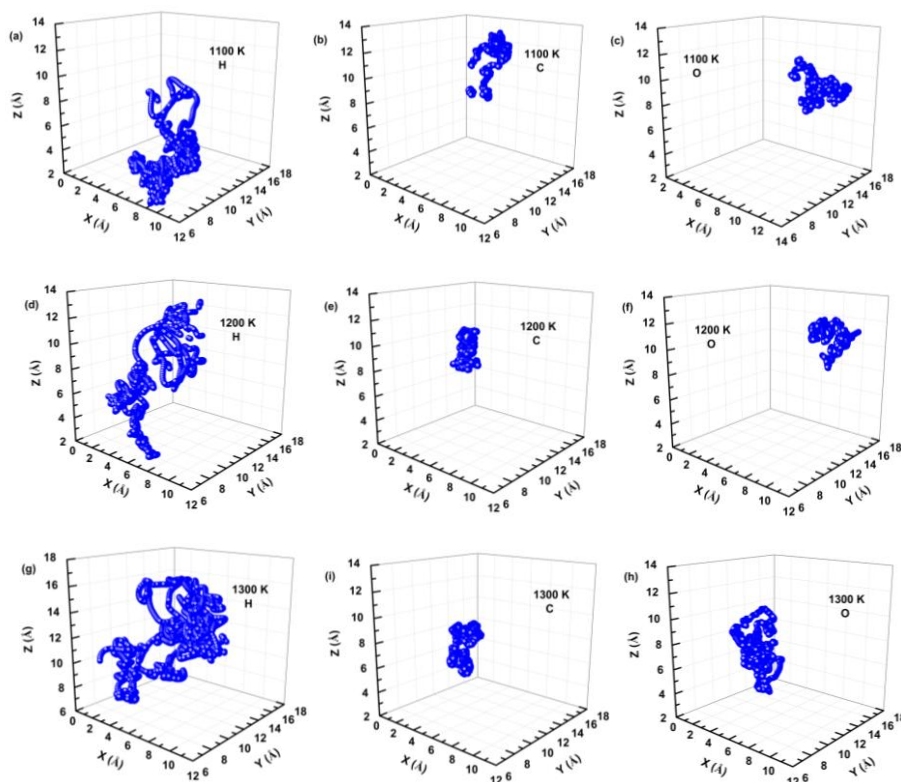
Fig. 4 The proton, carbon, and oxygen atom trajectories in the $(Li_2CO_3)_8$ cluster simulated at 1100 K, 1200 K, and 1300 K for 6 ps.
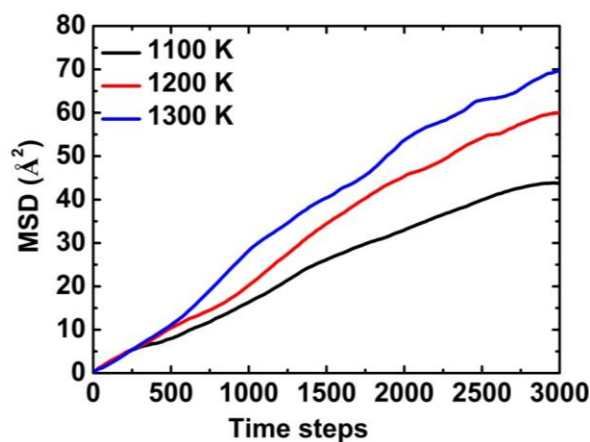
Fig. 5 The average mean square displacement (MSD) for proton transfer in the $(Li_2CO_3)_8$ cluster simulated at 1100 K, 1200 K, and 1300 K for 6ps.

Also, we can give the Arrhenius plot via Arrhenius relationship:

$$D(\text{T}) = D_0(\text{T})\exp(-\frac{\Delta E}{k_B T}) \qquad (4).$$

Herein, D_0 and ΔE are the pre-exponential and the diffusion barrier, respectively. k_B and T are the Boltzmann constant and absolute temperature, respectively. By fitting to the Arrhenius relationship over the temperature range, the pre-exponential and the effective activation barrier can be obtained. Fig. 6 shows the Arrhenius plot for proton transfer in the $(Li_2CO_3)_8$ cluster. From the slope of the straight line, the activation energy is calculated to be 6.4 kcal/mol, which is in good agreement with the energy barrier of proton transfer in inter-carbonate in the $(Li_2CO_3)_8$ clusters. This again supports that the proton fast transfer prefer in inter-carbonate and suggests that our cluster model is suitable to describe the state of molten carbonate.
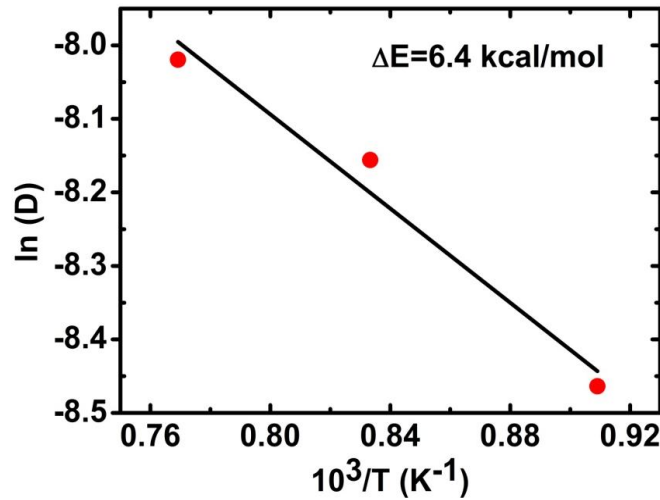

**Fig. 6 Arrhenius plots for proton transfer in the $(Li_2CO_3)_8$ cluster.**

2.4 Dynamic DFT on Proton Transfer in Bulk Lithium Carbonate

Additionally, we also simulate the proton migration in bulk lithium carbonate at finite temperatures by using FPMD. Since the system volume is adjusted due to the phase transition from crystal phase to molten phase, and only constant volume MD are possible at the moment for the standard first-principles molecular dynamics in the VASP program. So, we need to test the lattice constant for molten Li_2CO_3 structure. As described in theoretical details, we randomly chose a melt configuration, and then relax it for 20 ps (NVT) at different volume. Fig. 7 shows the average free energy versus the different lattice constant scale factors. We can see that there is small influence of volume on the free energy. The best lattice constant scale factor is 1.010, which means the volume expands 3.0 % after melting. In our following FPMD simulations, the lattice parameters of all structures multiply by 1.010 to obtain the accurate potential energy and free energy. Fig. 8 displays the structures of bulk lithium carbonate before and after melting. The molten lithium carbonate is simulated at 3000 K for 20 ps. Obviously the structures of bulk lithium carbonate after melting can represent the state of molten lithium carbonate.
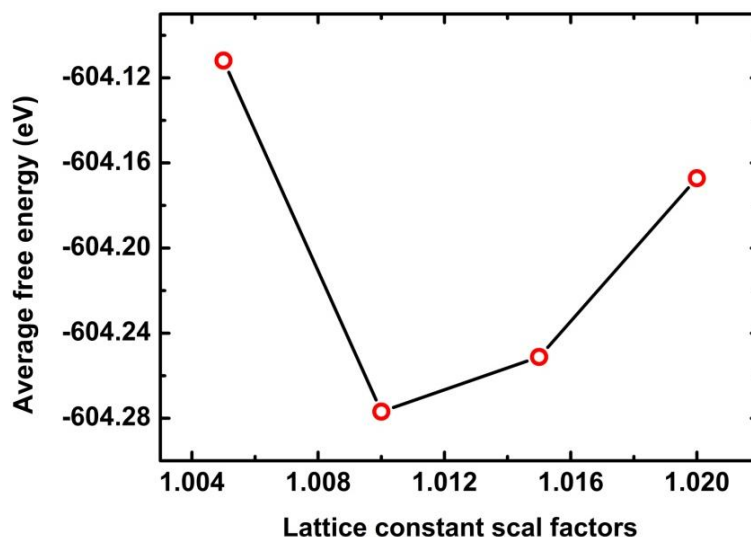
Fig. 7 The average free energy versus the lattice constant scale factors.
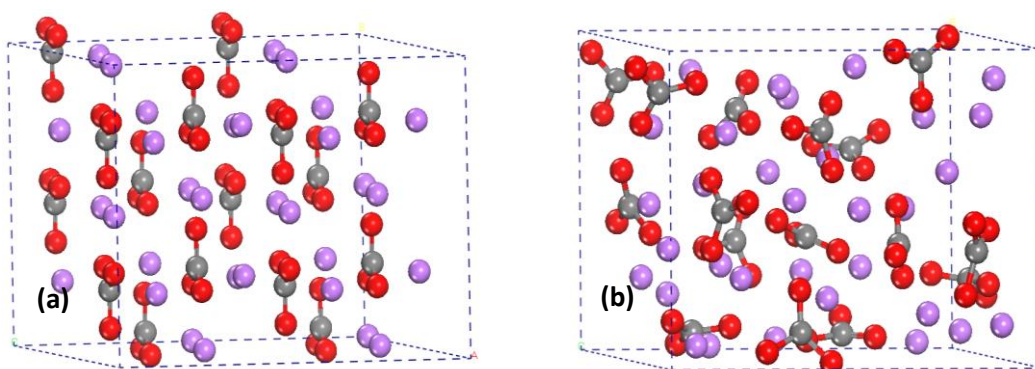
Fig.8 The structures of crystal (a) and molten phase (b), the latter is simulated at 3000 K.

Then, we randomly put one proton into the molten lithium carbonate and simulated at 1100 K, 1200 K, and 1300 K for 6ps, respectively. Fig. 9 shows a series of the snapshots of proton positions at 1200 K in a time interval of 1 ps for a total of 5 ps, the white ball represents one mobile proton. Comparison of proton positions at each snapshot indicates a fast proton diffusion as evidenced by the large change in displacement between each snapshot. The corresponding trajectory traces of proton as well as C and O ions are further depicted in Fig.10. It is evident that the proton transfer features like those in the $(Li_2CO_3)_8$ cluster: the trajectory of proton is very dispersed while the trajectory of carbon is very localized, and the trajectory of oxygen is somewhat localized. This indicates that the mechanism of proton transfer in the lithium molten carbonate is the same as in the $(Li_2CO_3)_8$ cluster: the proton fast transfers between the carbonate ions, at the same time, the carbonate ion adjust its position accordingly to reduce the energy barrier.
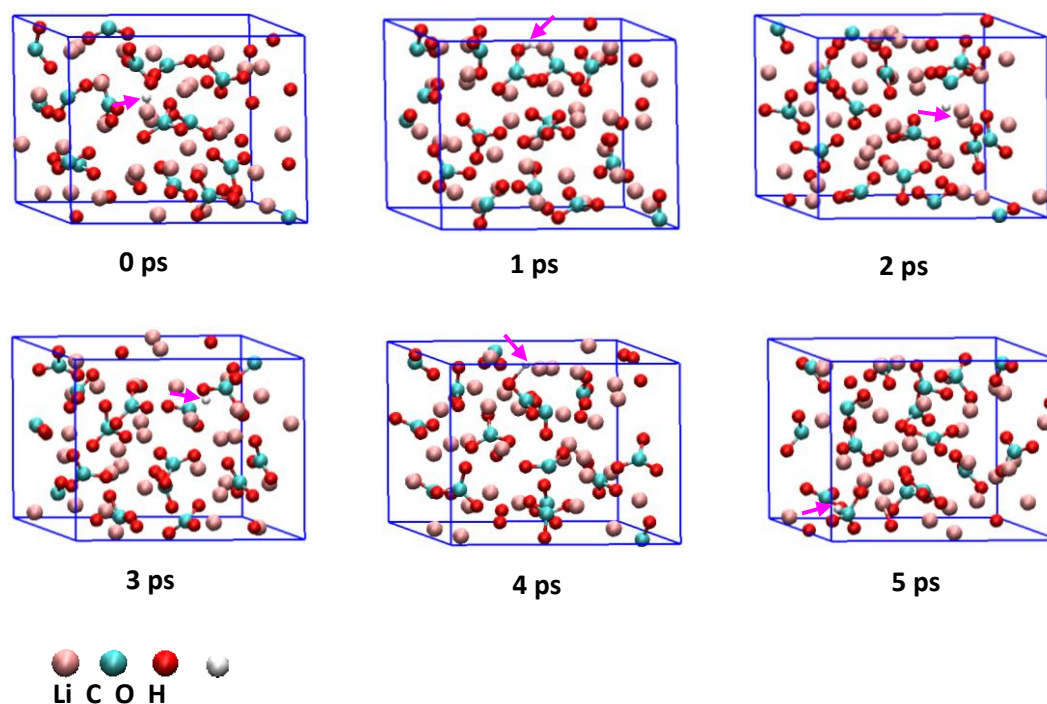
Fig. 9 The snapshots of proton diffusion in the lithium molten carbonate simulated at 1200 K. The white ball indicates the proton (denoted by arrow).
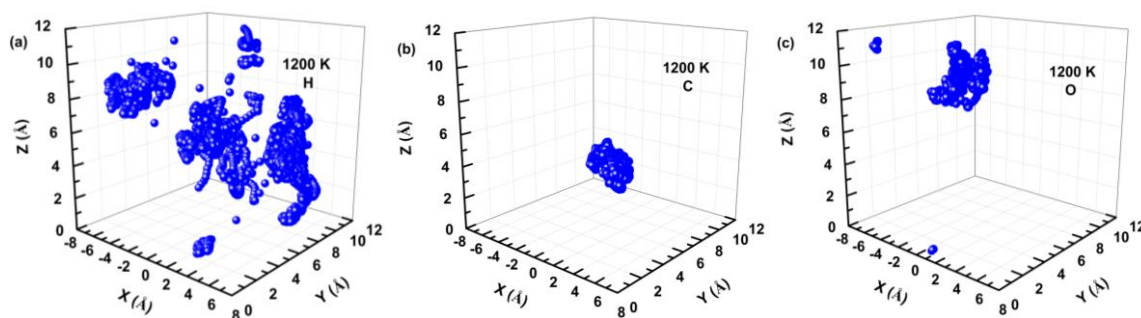
Fig. 10 The trajectories of proton, carbonate, and oxygen atoms in the lithium molten carbonate simulated at 1200 K for 6 ps.

Likewise, we also computed the mean square displacement (MSD) and Arrhenius plot. As shown in Fig. 11 and Fig.12, the features of MSD are similar to those in the $(Li_2CO_3)_8$ cluster: the MSD of proton increases linearly with time and the slope of MSD increases as the temperature increases, indicating a fast proton migration in the lithium molten carbonate. The activation energy is calculated to be 2.2 kcal/mol, which agrees well with that in the $(Li_2CO_3)_8$ cluster.

Such small activation energy again indicates that the proton transfer in the lithium molten carbonate is very facile and fast.
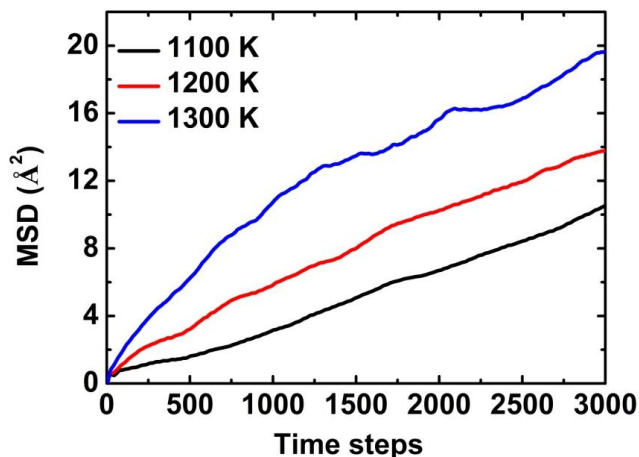
Fig. 11 The average mean square displacement (MSD) for proton transfer in the lithium molten carbonate simulated at 1100 K, 1200 K, and 1300 K for 6ps.
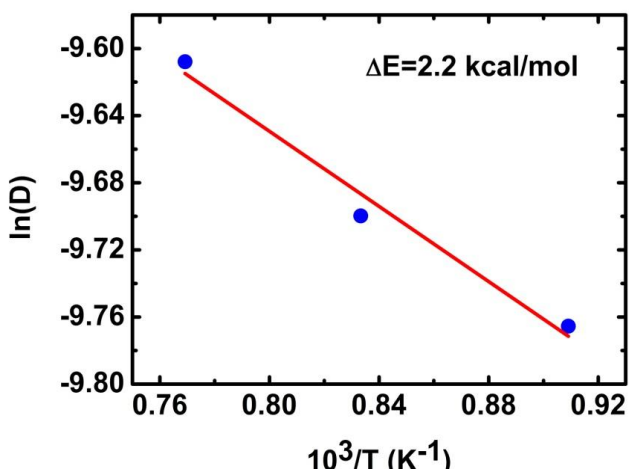
Fig. 12 Arrhenius plots for proton transfer in the lithium molten carbonate.

III. Conclusion and Future Work

In summary, the proton transfer in molten lithium carbonate has been systematically examined using DFT calculations. The transfer mechanism involves a concerted bond forming and breaking process. The inter-carbonate pathway is preferred than the intra path with calculated energy barrier of 1-8 kcal/mol and 40-50 kcal/mol, respectively. The DFT dynamic calculations confirmed the vitality of the inter-carbonate path. Calculated activation energy through Arrhenius plotting is 2.2 and 6.4 kcal/mol in MC cluater or bulk MC system, respectively. The analysis of atomic trajectory shows high mobility of proton, while carbonate atoms are largely limited and oxygen atoms with possible rotations to accept the proton. Our next goal is to examine the proton transfer at the surface of BYZ and the MC/BZY interface.

Theoretical Studies of Oxygen Reduction and Proton Transfer in SOFCs and Nerve Agents on Selected Surfaces

Jerry Whitten, North Carolina State University, Raleigh, NC 27695 (Co-PI)

PART C: Adsorption of Nerve Agents on Selected Surfaces

I. Overview of Research

In this work, we examine fundamental processes involving the interaction of nerve agents with solid surfaces using accurate electronic structure methods. Adsorption on several types of surfaces found in structural materials are considered for two types of nerve agents: sarin, a nerve gas, (see Fig. 1) and VX type nerve agents . Although both nerve agents are organophosphates, they differ in the ester linkage and in substituent groups. These differences are known to lead to different persistence times on surfaces.

Fig. 1. Sarin nerve gas. An organo-phosphate nerve agent with an ester linkage to an aliphatic group.
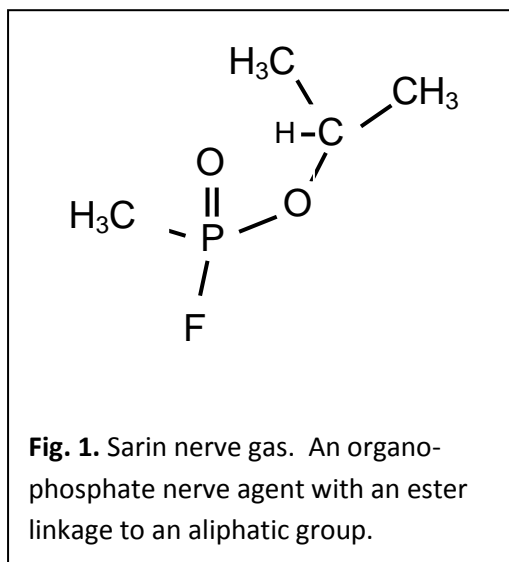
The objective of the work is to describe surface interactions and low energy electronic states at high aaccuracy using theory in order to understand the details of bonding to surfaces. The plan is to carry out the study so that factors that affect desorption energies, desorption kinetics and the spectral features of adsorbed nerve agents can be quantified. Understanding exactly how these molecules interact with a variety of solid surfaces is the primary goal of this work.

The project is divided into three phases:

1) Adsorption of sarin on hydrocarbon and oxide surfaces

2) Solvation of sarin adsorbed on surfaces by water

3) Study of the nerve agent VX and examination of the low lying excited states of sarin adsorbed on surfaces.

Phase 1 has been completed and Phase 2 is nearing completion. The project benefitted from the participation of two sabbatical leave visitors to the Whitten group from Athens, Greece, G. Petsalakis and I. Petsalakis. The visitors had prior experience using Density Functional Theory to describe molecule-surface interactions and this permitted a comparison of DFT and our many-electron CI calculations for sarin bound to hydrocarbon and oxide surfaces.

Appendix I contains the manuscript describing the results from Phase 1 of the project. This manuscript was submitted to J. Phys. Chem. and is currently undergoing minor revision to clarify questions raised in the review.

In the Phase 2 solvation studies, the surfaces are either initially coated by water, see for example the snapshot in Fig. 2, followed by introduction of sarin at a series of distances from the surface, or the sarin molecule is solvated first, see Fig. 3, and then allowed to approach the surface. In both cases, sarin and the surface compete for the water molecules and the molecules move optimally to solvate both sarin and the surface as the molecule approaches the surface. We follow the energetics of the system as a function of the distance of sarin from the surface allowing the water molecules to move to their minimum energy location for each choice of sarin position. The results should lead to an understanding of the effect of water solvation on the ability of a surface to retain sarin.
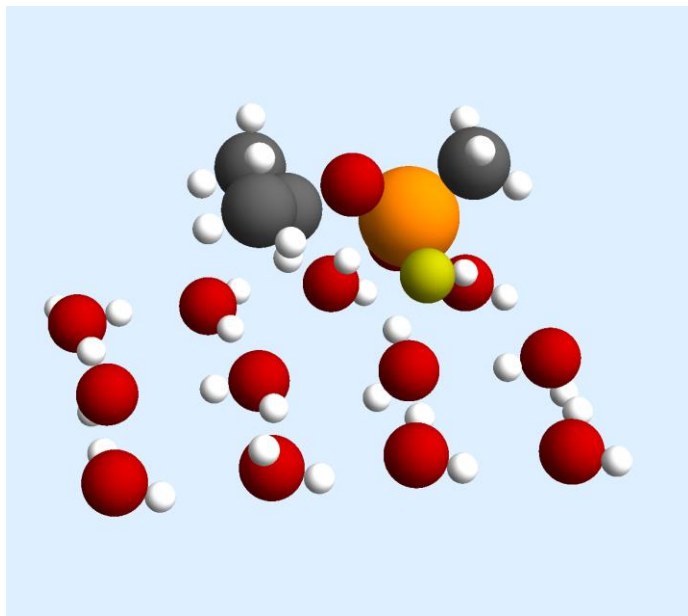

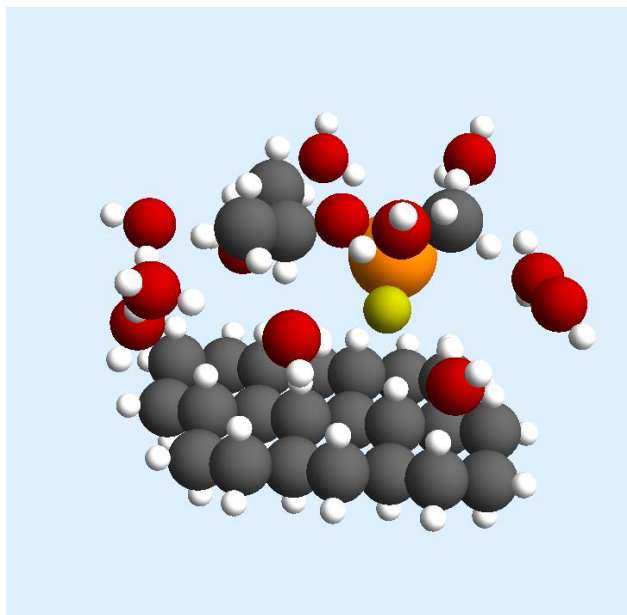Fig. 2. Binding directly to water layer: 16 kcal/mol

Fig. 3. Solvation of sarin near an aliphatic hydrocarbon surface by water.

II. Theoretical Methods

Two types of electronic structure approaches are employed: the first one involves configuration interaction along with a simplex optimization method for the geometry optimizations. The second approach involves density functional theory (DFT) calculations for the ground electronic state and time dependent DFT (TDDFT) calculations for excited electronic states, with details given below.

2.1 Many-electron CI Theory

The adsorbate-surface systems will be described by a configuration interaction embedding method that is designed to give an accurate many-electron description of the adsorbate-surface region for both ground and excited electronic states. Many applications to adsorbates on metals and oxides have been reported previously and details can be found in Ref. 18-21. In the case of small particles, there is no need to make approximations in the coupling of the local region to the bulk and in this case "embedding" refers to the creation of an electronic subspace that is treated by configuration interaction. A brief summary of the theory is given below.

Calculations are carried out for the full electrostatic Hamiltonian of the system

$$H = \sum_{i}^{N} [-\tfrac{1}{2}\nabla_i^2 + \sum_{k}^{Q}(\frac{-Z_k}{r_{ik}})] + \sum_{i<j}^{N} \frac{1}{r_{ij}}$$

Wavefunctions are constructed by self-consistent-field (SCF) and multi-reference configuration interaction (CI) expansions, $\Psi = \sum_{k} c_k (n!)^{-\frac{1}{2}} det(\chi_1^k \ \chi_2^k \cdots \chi_n^k) = \sum_{k} c_k \Phi_k$

Single and double excitations from an initial representation of the state of interest, Φ_r, are carried out to create a small CI expansion,

$$\Psi_r{}' = \Phi_r + \Sigma_{ijkl}\, \lambda_{ijkl}\, \Gamma_{ij\rightarrow kl}\, \Phi_r \; = \; \Sigma_m\, \Phi_m$$

Configurations, Φ_k, are retained if the interaction with Φ_r satisfies a relatively large threshold condition

$$|< \Phi_k\, |\, H\, |\, \Phi_r >|^{\,2} /\, |E_k - E_r|\quad > \quad 10^{-4}\; a.u.$$

Next, we refine the description of the state by generating a large CI expansion, Ψ_r, by single and double excitations from all important members of $\Psi_r{}'$ (those with coefficient > 0.05) to obtain

$$\Psi_r = \Psi_r{}' \; + \; \Sigma_m\, [\Sigma_{ik}\, \lambda_{ikm}\, \Gamma_{i\rightarrow k}\, \Phi_m \; + \; \Sigma_{ijkl}\, \lambda_{ijklm}\, \Gamma_{ij\rightarrow kl}\, \Phi_m]$$

where Φ_m is an important member of $\Psi_r{}'$. The additional configurations are generated by identifying and retaining all configurations, Φ_k, that interact with $\Psi_r{}'$ such that

$$|< \Phi_k\, |\, H\, |\, \Psi_r{}' >|^{\,2} /\, |E_k - E_r|\quad > \quad 3\times 10^{-7}\; a.u.$$

For this small threshold, typically 4×10^{4} configurations occur in the final CI expansion, and the expansion can contain single through quadruple excitations from an initial representation of the state $\Box_r$. Contributions of configurations not explicitly retained are estimated using perturbation theory.

In order to accelerate the convergence of the CI expansion results with respect to active space size for the excited state calculations, the molecular orbitals of the lowest triplet state for each system are first put through a unitary transformation. This transformation creates a set of occupied and virtual orbitals which have maximal exchange interaction with the occupied orbitals within the active space. The primary function of this is to allow accurate description of the states of interest in the presence of less accurately described lower-lying states. The basis of this argument lies in the way other configurations are generated from the states of interest. For a given excited state, $\Box_r$, allowing all single and double excitations from its important configurations also generates all lower lying states that have significant interaction with $\Box_r$. Since these configurations are in principle included in the diagonalization, it follows that the excited state, $\Box_r$, is orthogonal to and non-interacting with lower energy states. Thus the variational theorem for excited states is satisfied.

For the CI computations, the interaction of sarin is described using fixed-geometry surfaces sufficiently large enough to ensure that sarin would remain fully over the surface and not interact appreciably with boundary atoms. These surface models, depicted in a subsequent figure, correspond to $C_{22}H_{12}$ for graphene, $C_{22}H_{34}$ for graphane, and $Ca_{15}O_{15}$ for calcium oxide.

Compact, but still flexible bases were used in this study, and can roughly be characterized as double-zeta plus polarization.[22] These are described as $(10s5p1d)\rightarrow[4s2p1d]$ for C and O, $(12s8p1d)\rightarrow[6s4p1d]$ for P, $(10s5p)\rightarrow[4s2p]$ for F, and $(5s1p)\rightarrow[2s1p]$ for H. For the graphane surface only the p_z orbital was added to each H atom to ensure sufficient bond polarization. Graphene hydrogen atoms did not use any p functions, while the carbon atoms had additional diffuse s and p_z functions added with exponents of 0.08. For calcium oxide the surface should show little reaction to the addition of sarin and so a $(22s12p)\rightarrow[5s2p]$ basis for Ca and a

(12s5p)→[2s1p] basis for O were used. This basis was generated by minimizing the total energy of Ca_4O_4, and is given in the supplemental information.

2.2 Simplex Optimization Method

The CI geometry optimizations are carried out by the Nelder-Mead simplex procedure.[23] The optimization allows variation of the geometry of adsorbates on the surfaces of interest. In the simplex procedure, the parameters that define the geometry are taken as components of a so-called vertex or n-tuple. The energy is calculated for that vertex and a systematic variation of the parameters is carried out in a way that eliminates the worst vertex after each iteration. The procedure is widely used in applied mathematics and is surprisingly robust. It has an advantage in that energy gradients are not required and the energy minimization can be carried out directly at the CI level of theory since only a computer code capable of computing the energy is needed. The latter point is important when electron correlation has a significant effect on the geometry, e.g., stretched bonds or pre-dissociation. Geometry optimizations at the CI level allowed all degrees of freedom of sarin to vary, while keeping the model surfaces locked at a standard geometry.

2.3 DFT and TDDFT Calculations

Complementary to the CI calculations described in Section 2.1 DFT[24] and TDDFT[25] calculations employing the M062X functional[26, 27] and two types of basis sets, 6-31G(d,p) and 6-311G+(d,p) (i.e. including diffuse functions) have been carried out on sarin adsorbed on graphene, graphane and CaO, as in the CI calculations but using slightly different models for the surfaces. The smaller basis set was employed for larger models of the surfaces, cf., structures (a) and (d) for graphene ($C_{66}H_{22}$) and graphane ($C_{66}H_{88}$), respectively, and structure (g) for CaO in Figure 3. The larger basis set was employed for smaller models of the graphene ($C_{28}H_{14}$) and graphane ($C_{28}H_{42}$) surfaces, (b) and (e), respectively, in Figure 3, and also for the CaO ($Ca_{15}O_{15}$) surface, (h). Binding energies of sarin on the three surfaces have been determined, taking into account the basis superposition error. In addition, excited states and absorption spectra of the adsorption complexes of sarin on graphene and graphane have been calculated and compared to the absorption spectrum of free sarin obtained by TDDFT/M062X/6-311+G(d,p). For further comparison, the absorption spectrum of isolated sarin has been calculated by TDDFT employing nine additional functionals (specified in Figure 4) and the 6-311+G(d,p) basis set. Corresponding data has been generated by CI calculations for free sarin as well as the adsorption complexes.

Geometry optimization of the adsorption complexes involved first the optimization of the surface and subsequently optimization of the adsorbed sarin. In the case of CaO, inclusion of 5 atoms on the surface in the second step of the optimization resulted in 2.3 kcal/mol increased binding energy.

Finally, DFT/M062X calculations have also been carried out for sarin on MgO ($Mg_{15}O_{15}$) (cf. (h) in Figure 3), for comparison with previous work on this system.[6] For these calculations basis sets 6-31G(d,p) and 6-311G(d,p) have been employed. Addition of diffuse functions was not possible as the calculations did not converge. For comparison, the previous work employed 6-31G(d) basis set with DFT/B3LYP and MP2 calculations on different models of sarin on MgO.[6] All the DFT and TDDFT calculations of the present work have been carried using Gaussian 09.[28]

III. Results and Discussions

3.1 Sarin Geomerties

Four conformers of sarin were optimized at the CI level. The minimum energy structure of sarin used in the present study is depicted in Figure 1. This is the geometry labeled sarin II reported in Ref. 17. The energy of this geometry is less than 1 kcal/mol above the minimum energy geometry reported in Ref. 17, and thus for the purposes of this research is considered unimportant. The remaining conformers differed by rotation of the aliphatic and phosphate regions and changes in the central C-O-P bond angle.

3.2 Binding Geometries

3.2.1 Overview

In Figure 3 the structures of the adsorption complexes obtained by DFT and CI are given; in Table 1 the calculated binding energies are collected. These results will be discussed below starting with the comparatively simplest case of sarin on CaO.
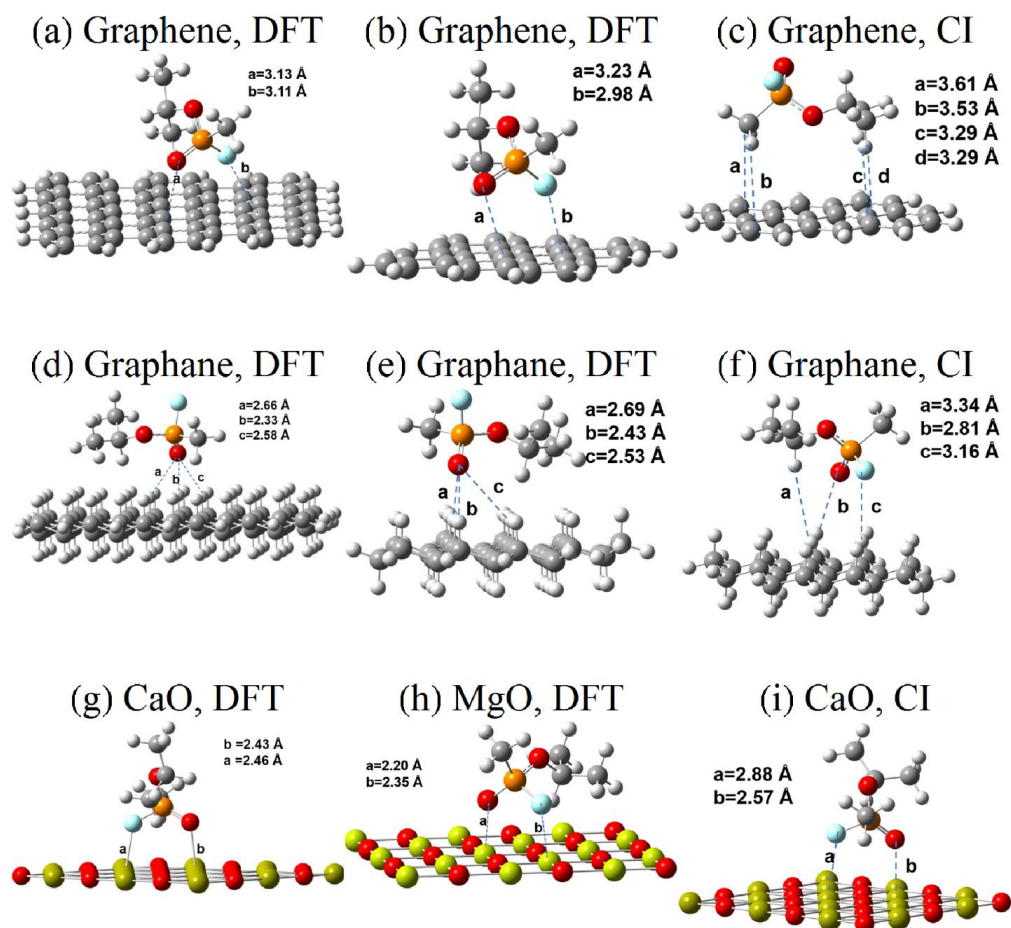
Figure 3. Optimum geometries of the adsorption complexes of sarin on graphene, (a) and (b) obtained by DFT and (c) by CI, on graphane, (d) and (e) by DFT and (f) by CI, on CaO, (g) by DFT and (i) by CI and on MgO (h) by DFT, cf. text.

3.2.2 Sarin on CaO

Figures 3g–i show optimal binding geometries of sarin to oxide surfaces. The binding appears to be a straight-forward electrostatic interaction. The P atom of sarin aligns with an O atom of the surface, and the F and terminal O atoms align over Ca atoms, creating pairs of opposite charges. The center of mass of sarin is 4.04 Å above the surface in the CI calculations. In all calculations, the Ca-O/F distance is on the order of 2.4 Å. All calculations are in good agreement on the binding energy (Table 1), with all results in the range of 10–20 kcal/mol. Relaxation of the CaO lattice during binding was found to have negligible impact on the binding energy using DFT. For comparison, reported values of binding energy of sarin on MgO, calculated by B3LYP/6-31G(d) and a large model ($Mg_{16}O_{16}$) is 2.9 kcal/mol while that obtained by MP2/6-31G(d) and a small cluster (Mg_4O_4) is 50 kcal/mol.[6] It should be noted that in the present work the MgO was modelled with M062X on a single layer of $Mg_{15}O_{15}$, not two layers as in the previous work. As shown in Table 1, significant binding of 20.0 kcal/mol is obtained for sarin on MgO, consistent with the expectation of stronger binding of sarin to MgO than CaO.

Table 1. Calculated binding energy (BE) of sarin at different surfaces by DFT and CI.

Surface (structure of Figure 3) /basis set	BE (kcal/mol)	BSSE-corrected BE (kcal/mol)
Graphene (**a**)/ 6-31G(d,p)	6.7	-
Graphene (**b**)/ 6-31G(d,p)	6.4	2.6
Graphene (**b**)/ 6-311+G(d,p)	8.2	4.8, 5.2*
Graphane (**d**)/ 6-31G(d,p)	9.0	-
Graphane (**e**)/ 6-31G(d,p)	7.9	4.9
Graphane (**e**)/ 6-311+G(d,p)	8.5	6.4, 2.4*
CaO (**g**)/ 6-31G(d,p)	33.9	16.1
CaO (**g**)/ 6-311+G(d,p)	22.3	18.8, 13.2*
MgO (**h**)/6-31G(d,p)	32.8	19.3
MgO (**h**)/6-311G(d,p)	31.8	20.0

*Corresponding CI value

3.2.3 Sarin on graphene

Unlike the results for CaO, DFT and CI give different binding geometries for sarin on graphene (Figure 3a–c). Specifically, DFT models predict binding through the sarin oxygen and fluorine atoms, while CI predicts a flipped orientation, cf. Figure 3b vs 3c. Consistency between the M062X/6-31G(d,p) results for large (Fig. 3a) and middle-sized (Fig 3b) graphene surfaces suggests that the M062X/6-311+G(d,p) binding energy of 4.8 kcal/mol should be taken as accurate. Despite the difference in orientation, there is good agreement with the CI computed binding energy of 5.2 kcal/mol. Cross-examinations of the two orientations with the two levels of theory indicate that the energy difference between the two orientations is small (about 0.1–0.4 kcal/mol, depending on the model), with the optimum geometry being dependent on the particulars of the method used. It should be noted that in both orientations the dipole moment of sarin is directed perpendicular to the graphene surface.

3.2.4 Sarin on graphane

Of the three surfaces modelled, graphane exhibits the greatest discrepancy between the DFT and CI results. From the DFT results, sarin binds with its oxygen atom down and 2.3 Å from a nearest surface hydrogen atom, and its fluorine atom pointed away from the surface (Fig. 3d,e). Predicted binding is on the order of 6 kcal/mol – slightly greater than that of sarin on graphene. The CI computations suggest a binding with the sarin oxygen and fluorine atoms at the surface (Fig. 3f), but a binding of only 2.4 kcal/mol. Investigation of the orientation of sarin on graphane obtained by CI employing the CI model ($C_{22}H_{34}$), as well as the larger ($C_{28}H_{42}$) model, using the DFT/M062X method show that for the smaller CI model only the CI structure (cf. (f) of Figure 3) is obtained whereas with the larger model the DFT structure, cf. (e) in Figure 3, is favored. Therefore there is a significant effect of the size of the model employed on the calculated orientation of the adsorption complex.

3.3 Excited States

A great deal of experimental and theoretical work has been devoted to the determination of the lowest energy structure of sarin and other warfare agents in the ground electronic state, but the excited states have not been studied very extensively.[5] For sarin, a low intensity absorption is reported with the threshold electronic excitation occurring in the vacuum-UV (~7.1 eV or higher) with varying theoretical estimates, eg. 7.38 eV obtained by TDDFT/B3LYP/6-311+G(2df,p) and 9.9 eV by MP2/6-31+G(d) calculations.[9] Here too we find a varying excitation energy for the lowest singlet excited state of free sarin, depending on the functional employed in TDDFT/6-311+G(d,p) calculations . In Figure 4 the absorption spectra of free sarin obtained by TDDFT calculations and ten different functionals, offered in Gaussian 09, are shown. The lowest onset for the electronic excitations is obtained with the PBEPBE functional at 6.6 eV and the highest with M062X at 8.1 eV. Generally low oscillator strengths are calculated with all functionals employed. CI calculations on the excited state employing the basis set previously described lead to an excitation energy of 9.1 eV, i.e., comparable to an earlier MP2/6-31+G(d) result.[9] However, inclusion of a single diffuse s function (exponent of 0.01) in the phosphorus atom basis set allows an accurate CI estimate of the lowest Rydberg excitations. These come in at 8.0 eV and 8.5 eV, corresponding to excitations from the oxygen/fluorine lone-pair manifold into a Rydberg state. This is in good agreement with the present CAM-B3LYP and M062X TDDFT results on the spectrum of free sarin, cf. Figure 4.

Next, the absorption spectra of sarin adsorbed on graphene and graphane were considered using TDDFT/M062X and the 6-311+G(d,p) basis set. For the graphene-sarin system the lowest 50 roots were calculated in the region 1.98 eV – 6.19 eV, none of which correspond to the sarin-sarin excitation. The lowest transitions correspond to graphene-graphene excitations. There also exist a number of charge-transfer type excitations, from occupied orbitals of graphene to unoccupied orbitals of sarin. For example, states calculated at 3.37 and 4.2 eV involve excitations into a Rydberg unoccupied orbital of sarin. Other such states are found at 5.5, 6.08, 6.18 and 6.19 eV. The calculations on graphane-sarin involved the lowest 20 roots. In this case the lowest unoccupied orbital or LUMO is a Rydberg orbital of sarin and is involved in several excited states of the complex. In particular, the lowest excited state at 6.4 eV, which is characterized by the HOMO→LUMO excitation, corresponds to an excitation from graphane to sarin. As was the case for graphene-sarin, the calculations did not reach any sarin-sarin excited states. It should be noted that the above calculations on the excited states of the adsorption

complexes, just as in the case of free sarin, required inclusion of diffuse functions in the basis set. With the 6-31G(d,p) basis set the first 25 roots of the CaO-sarin calculation correspond to excitations involving only the surface. Calculations with the 6-311+G(d,p) basis on the CaO-sarin complex were not practical.
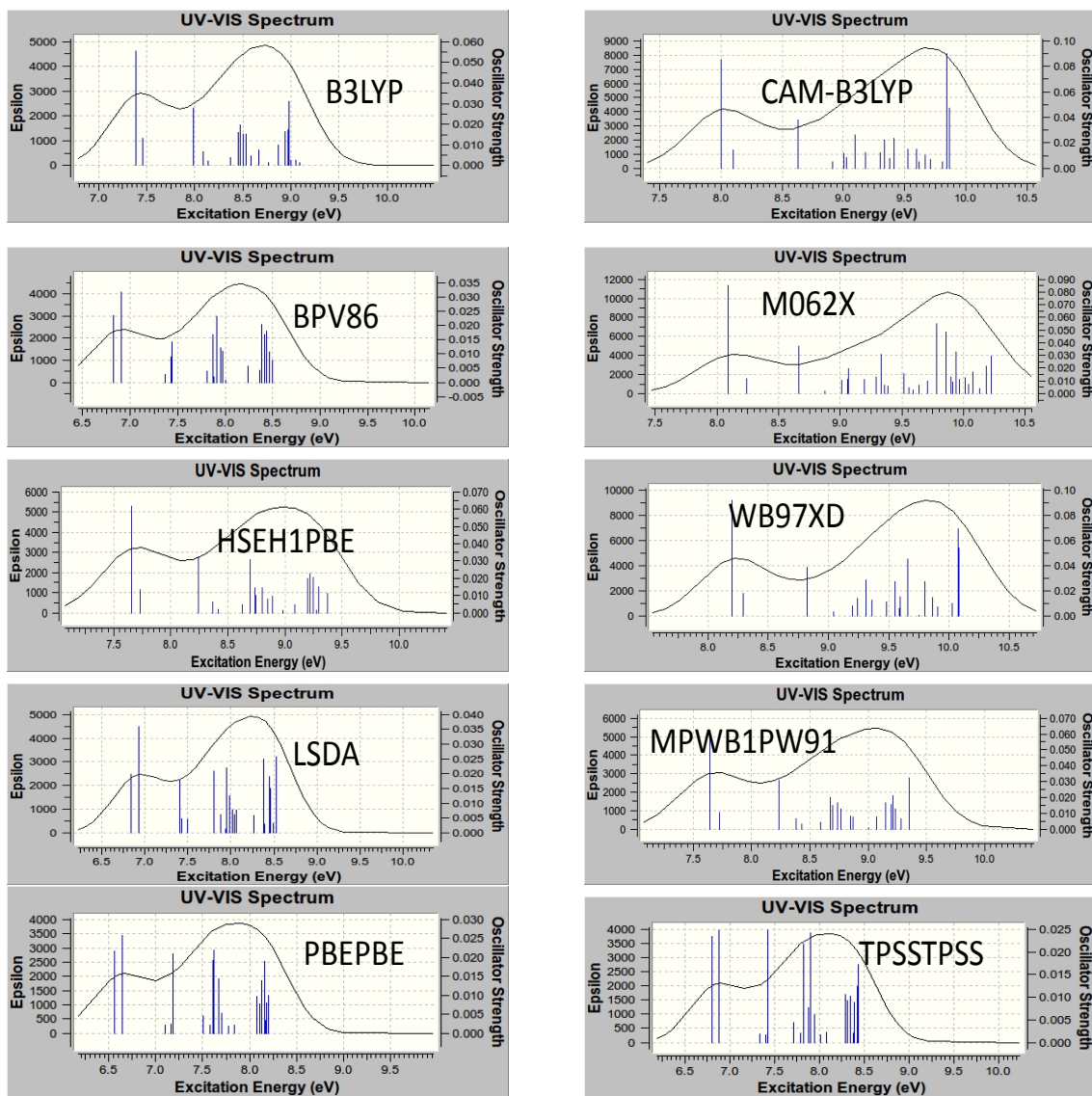
Figure 4. Adsorption spectra of free sarin calculated by TDDFT employing different functionals, as indicated.

CI Computations in which the dominant component of the excitation was restricted to be into the Rydberg orbital of sarin were used to determine the transition energy of the lowest lying surface-to-sarin electron transfer excitation. For graphane, the lowest is at 7.0 eV; the remainder are above the free sarin excitation. The numerous low-lying virtual orbitals on graphene proved a significant challenge for isolating the charge-transfer excitation, and the best estimate places it

near 5.3 eV. Excitations from the central portion of the CaO model surface (excitations from orbitals localized on the edges of the model were disallowed) provided a set of ten electron-transfer possibilities ranging in transition energy from 6.2 eV to 8.5 eV. Therefore, with both methods, the existence of charge-transfer excited states at energies lower than the sarin-sarin excitation is indicated. Similar observations have been reported for sarin and other organophosphorus warfare agents adsorbed on a γ-Al_2O_3 surface.[5]

IV. Summary

Our results indicate that the polarized phosphate region of the sarin molecule plays a critical role in its binding to aliphatic, aromatic, and oxide surfaces. Specifically, the Lewis-base portion acts as the binding agent. For the surfaces considered in the present study, only those that are ionic (CaO) or have large polarizability (graphene) give strong binding for sarin. Binding to aliphatic surfaces is weak. Figure 5 depicts CI potential curves for interaction of sarin with the three model surfaces.
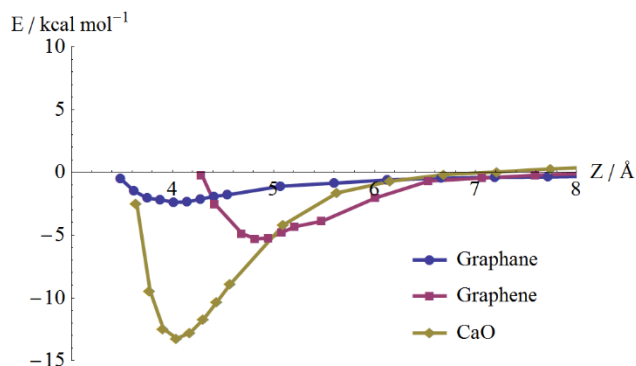
Figure 5. Potential curves for sarin interaction with three model surfaces. Infinite separation limit is free sarin in minumum energy geometry and bare surface. The z-axis corresponds to the height of the sarin center-of-ma

ss above the highest atom of surface.

It is concluded that

- Sarin binds to graphane, graphene, and calcium oxide surfaces by 2.4, 5.2, and 13.2 kcal/mol, respectively according to CI, with corresponding DFT binding energies 6.4, 4.8, and 18.8 kcal/mol, respectively.

- Free sarin has an excitation into a Rydberg state at about 8 eV.

- Each of the three surfaces studied is capable of transferring an electron to sarin at or below the sarin Rydberg excitation. Both DFT and many-electron computational methods gave similar results, with TDDFT capable of determining a greater total number of roots, and CI capable to giving accurate results for specific states of interest.

V. REFERENCES (Part C Only)

1.   Wilmsmeyer, A. R.; Gordon, W. O.; Davis, E. D.; Troya, D.; Mantooth, B. A.; Lalain, T. A.; Morris, J. R., Infrared Spectra and Binding Energies of Chemical Warfare Nerve Agent

Simulants on the Surface of Amorphous Silica. *Journal of Physical Chemistry C* 2013, 117, 15685-15697.

2.   Troya, D.; Edwards, A. C.; Morris, J. R., Theoretical Study of the Adsorption of Organophosphorous Compounds to Models of a Silica Surface. *Journal of Physical Chemistry C* 2013, 117, 14625-14634.

3.   Kowalczyk, P.; Gauden, P. A.; Terzyk, A. P.; Neimark, A. V., Screening of carbonaceous nanoporous materials for capture of nerve agents. *Physical Chemistry Chemical Physics* 2013, 15, 291-298.

4.   Patil, L. A.; Bari, A. R.; Shinde, M. D.; Deo, V.; Kaushik, M. P., Detection of dimethyl methyl phosphonate - a simulant of sarin: The highly toxic chemical warfare - using platinum activated nanocrystalline ZnO thick films. *Sensors and Actuators B-Chemical* 2012, 161, 372-380.

5.   Bermudez, V. M., Computational Study of Environmental Effects in the Adsorption of DMMP, Sarin, and VX on gamma-Al2O3: Photolysis and Surface Hydroxylation. *Journal of Physical Chemistry C* 2009, 113, 1917-1930.

6.   Michalkova, A.; Ilchenko, M.; Gorb, L.; Leszczynski, J., Theoretical study of the adsorption and decomposition of sarin on magnesium oxide. *Journal of Physical Chemistry B* 2004, 108, 5294-5303.

7.   Michalkova, A.; Paukku, Y.; Majumdar, D.; Leszczynski, J., Theoretical study of adsorption of tabun on calcium oxide clusters. *Chemical Physics Letters* 2007, 438, 72-77.

8.   Paukku, Y.; Michalkova, A.; Leszczynski, J., Adsorption of dimethyl methylphosphonate and trimethyl phosphate on calcium oxide: an ab initio study. *Structural Chemistry* 2008, 19, 307-320.

9.   Rauk, A.; Shishkov, I. F.; Vilkov, L. V.; Koehler, K. F.; Kostyanovsky, R. G., DETERMINATION OF THE STRUCTURE AND CHIROPTICAL PROPERTIES OF THE PARENT NERVE-GAS O-METHYL METHYLPHOSPHONOFLUORIDATE BY AB-INITIO CALCULATIONS, ELECTRON-DIFFRACTION ANALYSIS, AND NMR-SPECTROSCOPY. *Journal of the American Chemical Society* 1995, 117, 7180-7185.

10.   Koskela, H., A set of triple-resonance nuclear magnetic resonance experiments for structural characterization of organophosphorus compounds in mixture samples. *Analytica Chimica Acta* 2012, 751, 105-111.

11.   Christesen, S. D.; Jones, J. P.; Lochner, J. M.; Hyre, A. M., Ultraviolet Raman Spectra and Cross-Sections of the G-series Nerve Agents. *Applied Spectroscopy* 2008, 62, 1078-1083.

12.   DaBell, R. S.; Suenram, R. D.; Lavrich, R. J.; Lochner, J. M.; Ellzy, M. W.; Sumpter, K.; Jensen, J. O.; Samuels, A. C., The geometry of organophosphonates: Fourier-transform microwave spectroscopy and ab initio study of diethyl methylphosphonate, diethyl ethylphosphonate, and diisopropyl methylphosphonate. *Journal of Molecular Spectroscopy* 2004, 228, 230-242.

13.   Mott, A. J.; Rez, P., Calculated infrared spectra of nerve agents and simulants. *Spectrochimica Acta Part a-Molecular and Biomolecular Spectroscopy* 2012, 91, 256-260.

14.   Zuo, G.-M.; Cheng, Z.-X.; Shi, W.-P.; Zhang, X.-H.; Zhang, M., Photoassisted removal of sarin vapor in air under UV light irradiation. *Journal of Photochemistry and Photobiology a-Chemistry* 2007, 188, 143-148.

15.   Zuo, G.-M.; Cheng, Z.-X.; Li, G.-W.; Shi, W.-P.; Miao, T., Study on photolytic and photocatalytic decontamination of air polluted by chemical warfare agents (CWAs). *Chemical Engineering Journal* 2007, 128, 135-140.

16.   Xu, C.-X.; Zuo, G.-M.; Cheng, Z.-X.; Han, J., Computational Study Toward Understanding the Photodissociation Mechanism of Sarin. *International Journal of Quantum Chemistry* 2011, 111, 4410-4417.

17.   Kaczmarek, A.; Gorb, L.; Sadlej, A. J.; Leszczynski, J., Sarin and soman: Structure and properties. *Structural Chemistry* 2004, 15, 517-525.

18.   Papas, B. N.; Whitten, J. L., Dissociation of Water on a Palladium Nanoparticle. *International Journal of Quantum Chemistry* 2010, 110, 3072-3079.

19.   Papas, B. N.; Whitten, J. L., Silver as an electron source for photodissociation of hydronium. *Journal of Chemical Physics* 2011, 135.

20.   Papas, B. N.; Whitten, J. L., Excitonic states in a (Ti6O12)(3) nanotube. *Journal of Chemical Physics* 2013, 138, 6.

21.   Whitten, J. L.; Yang, H., Theory of chemisorption and reactions on metal surfaces. *Surface Science Reports* 1996, 24, 59-124.

22.   Whitten, J. L., Gaussian Lobe Function Expansions of Hartree-Fock Solutions for First-Row Atoms and Ethylene. *Journal of Chemical Physics* 1966, 44, 359-&.

23.   Nelder, J. A.; Mead, R., A SIMPLEX-METHOD FOR FUNCTION MINIMIZATION. *Computer Journal* 1965, 7, 308-313.

24.   Parr, R. G.; Yang, W. T., DENSITY-FUNCTIONAL THEORY OF THE ELECTRONIC-STRUCTURE OF MOLECULES. *Annual Review of Physical Chemistry* 1995, 46, 701-728.

25.   Marques, M. A. L.; Gross, E. K. U., Time-dependent density functional theory. *Annual Review of Physical Chemistry* 2004, 55, 427-455.

26.   Zhao, Y.; Truhlar, D. G., Density functionals with broad applicability in chemistry. *Accounts of Chemical Research* 2008, 41, 157-167.

27.   Zhao, Y.; Truhlar, D. G., The M06 suite of density functionals for main group thermochemistry, thermochemical kinetics, noncovalent interactions, excited states, and transition elements: two new functionals and systematic testing of four M06-class functionals and 12 other functionals. *Theoretical Chemistry Accounts* 2008, 120, 215-241.

28.   Frisch, M. J.; Trucks, G. W.; Schlegel, H. B.; Scuseria, G. E.; Robb, M. A.; Cheeseman, J. R.; Scalmani, G.; Barone, V.; Mennucci, B.; Petersson, G. A.; Nakatsuji, H.; Caricato, M.; Li, X.; Hratchian, H. P.; Izmaylov, A. F.; Bloino, J.; Zheng, G.; Sonnenberg, J. L.; Hada, M.; Ehara, M.; Toyota, K.; Fukuda, R.; Hasegawa, J.; Ishida, M.; Nakajima, T.; Honda, Y.; Kitao, O.; Nakai, H.; Vreven, T.; Montgomery, J. A., Jr.; Peralta, J. E.; Ogliaro, F.; Bearpark, M.; Heyd, J. J.; Brothers, E.; Kudin, K. N.; Staroverov, V. N.; Kobayashi, R.; Normand, J.; Raghavachari, K.; Rendell, A.; Burant, J. C.; Iyengar, S. S.; Tomasi, J.; Cossi, M.; Rega, N.; Millam, N. J.; Klene, M.; Knox, J. E.; Cross, J. B.; Bakken, V.; Adamo, C.; Jaramillo, J.; Gomperts, R.; Stratmann, R. E.; Yazyev, O.; Austin, A. J.; Cammi, R.; Pomelli, C.; Ochterski, J. W.; Martin, R. L.; Morokuma, K.; Zakrzewski, V. G.; Voth, G. A.; Salvador, P.; Dannenberg, J. J.; Dapprich, S.; Daniels, A. D.; Farkas, Ö.; Foresman, J. B.; Ortiz, J. V.; Cioslowski, J.; Fox, D. J. *Gaussian 09, Revision **D.01***, Gaussian, Inc.: Wallingford CT, 2009.